

8. SITE 978¹

Shipboard Scientific Party²

HOLE 978A

Date occupied: 1600, 15 June 1995
Date departed: 0230, 21 June 1995
Time on hole: 5 days, 10 hr, 30 min
Position: 36°13.867'N, 2°3.424'W
Drill pipe measurement from rig floor to seafloor (m): 1941.0
Distance between rig floor and sea level (m): 11.6
Water depth (drill pipe measurement from sea level, m): 1929.4
Total depth (from rig floor, m): 2639.0
Penetration (m): 698.0
Number of cores (including cores having no recovery): 53
Total length of cored section (m): 504.2
Total core recovered (m): 406.66
Core recovery (%): 80.7
Oldest sediment cored:
Depth (mbsf): 698.0
Nature: Claystone
Age: Miocene
Comments: Drilled from 0.0 to 213.0 mbsf spot coring Core 1R (110.3–119.9 mbsf) and Core 2R (168.4–178.0 mbsf).

Principal results: Site 978 (proposed Site Alb-4) is located in the Eastern Alboran Basin to the south of Cabo de Gata and 24 km north of Site 977. The site lies in an small east-west-trending basin within the same 35-km-wide graben as Site 977, but north of the Al-Mansour Seamount. Site 978 was selected because, like Site 977, seismic data at this site show a lower sequence that may represent the synrift sediments that filled the Eastern Alboran Basin, overlain by uniform, flat-layered sediments. We drilled Site 978 to complete objectives that were not achieved at Site 977: (1) to penetrate a major unconformity, which we were unable to penetrate at Site 977; and (2) to sample the underlying synrift sequence, in order to determine the age and nature of these deposits and to identify the relative proportions of synrift and postrift subsidence. In addition, Site 978 results, like Site 977, will permit accurate seismic correlation between the Alboran Sea Basin and the South Balearic Basin.

A continuous sequence of 485.3 m (from 213 to 694.3 mbsf) of upper Miocene (Zone NN11) to Pleistocene (Subzone NN19) sediments was recovered at Site 978. The Pliocene/Pleistocene boundary, as approximated by the first occurrence of *Gephyrocapsa oceanica*, is between 222.77 and 223.35 mbsf; the Miocene/Pliocene boundary occurs between 607.51 and 611.39 mbsf. All Miocene cores are assigned to Zone NN11 (Messinian or uppermost Tortonian). In the Pliocene interval, foraminifers are abundant and preservation is generally good. Miocene foraminifers are moderately to poorly preserved. Using foraminiferal and nannofossil ages and geomagnetic polarity events, sedimentation rates are 127 m/m.y. for the

Pleistocene, 111 m/m.y. for the upper Pliocene, 120 m/m.y. for the lower Pliocene, and 156 m/m.y. for the upper Miocene.

The sedimentary sequence sampled at Site 978 was divided into three lithologic units:

Unit I (213.0–620.9 mbsf). This unit consists of early Pleistocene to Pliocene grayish olive nannofossil clay to claystone that is variably bioturbated. Foraminifers and shell fragments are dispersed throughout the unit. The carbonate fraction consists predominantly of nannofossils, micrite, bioclasts, and foraminifers. Terrigenous components include quartz, feldspar, mica, sedimentary and low-grade metamorphic rock fragments, and accessory minerals such as garnet and zircon. Minor amounts of organic debris (up to 5%) and diagenetic opaque minerals (up to 3%) are present. On the basis of their distinct color, lithological associations, and sedimentary structures, three subunits have been distinguished within Unit I.

Unit II (620.9–630.67 mbsf). This unit consists of an upper Miocene gravel-bearing interval containing pebbles of volcanic and sedimentary rocks. The contact between Units I and II was not recovered. Some pebbles have smooth, rounded, weathered surfaces and some are partly coated by a thin microcrystalline calcareous laminae (zeolites and smectite), possibly representing matrix or cement. The pebbles are formed of andesitic basalt to andesite, chert, limestone, quartzite, and metamorphic rocks.

Unit III (630.67–694.3 mbsf). This unit consists of Miocene sandy and silty layers that exhibit parallel and cross lamination, and are inverse to normal grading. Sparse bioturbation and in situ brecciation and clastic dikes are observed throughout this unit.

Sediment bedding is mostly horizontal and occasional slump folding and small synsedimentary faults occur. Slump folds are well preserved near the base of the Pliocene. Late Miocene sediments are significantly more consolidated than the Pliocene sequence above. Bedding in the Miocene section is also mostly horizontal, but some units are cut by numerous dilational fractures with irregular orientations. The fractures possibly represent hydraulic fractures formed by overpressured and underconsolidated horizons within the sequence.

Carbonate content varies between 10% and more than 60% in the Pliocene sediments. Miocene sediments are distinctly lower in carbonate content. Total organic carbon (TOC) averages 0.3% and reaches values up to 0.9% in some organic-rich layers. Organic C/N ratios are mostly between 4 and 8. From Rock-Eval analysis we infer that the organic matter has been heavily oxidized, probably by microbial reworking.

Concentrations of headspace methane are high in sediments at Site 978. The source of the methane is probably in situ microbial fermentation of marine organic matter. Concentrations of propane, *iso*-butane, and *iso*-pentane exceed or equal those of ethane in sediments from about 300 mbsf to 500 mbsf. These C₃, C₄, and C₅ gases were probably produced by thermal degradation of sedimentary organic matter.

Interstitial water salinity, chloride, sodium, and calcium increase downhole with a steepening of the concentration gradients below 450 mbsf. Sulfate concentrations are close to zero until 450 mbsf and increase steeply below 500 mbsf. Because no halite salts are known at depth in this area, the high concentrations of these elements are likely derived from paleo-seawater or lateral migration of saline fluids from the Messinian halite deposits that are known to occur in the South Balearic Basin, about 30 km east of Site 978. The downhole lithium increase may also be partly related to "evaporitic" fluids. Alkalinity shows a maximum of 3.5 mM at 269.5 mbsf that corresponds to the highest ammonia concentrations, indicating that organic matter decomposition is most extensive at that depth. Magne-

¹Comas, M.C., Zahn, R., Klaus, A., et al., 1996. *Proc. ODP, Init. Repts.*, 161: College Station, TX (Ocean Drilling Program).

²Shipboard Scientific Party is given in the list preceding the Table of Contents.

sium concentrations are consistently below seawater concentrations, indicating precipitation of high-magnesium calcite or dolomite in the sediments. Strontium shows a maximum at 492.20 mbsf, likely indicating carbonate recrystallization.

At least 11 magnetic polarity zones are identified between 390 and 610 mbsf at Site 978. Correlation with biostratigraphic data suggests that these represent polarity subchron C2An.2n through subchron C3n.4n (3.22 to 4.98 Ma). A sharp increase in intensity occurs at 440 mbsf, about 50 m below the last well-defined polarity change. A similar increase in intensity was observed at Site 977 at 420 mbsf indicating good correlation between the two neighboring sites. Remanent directions, however, are substantially different between the sites, probably because of different coring techniques. RCB drilling at Site 978 resulted in the only reasonable magnetostratigraphy obtained during Leg 161, as well as better preservation of sediment structures and less intense biscuiting than at Site 977, which was drilled using XCB.

The post-Messinian stratigraphy established at Site 978 supports our results and interpretations from Site 977, and an accurate correlation between the post-Messinian sequence at both sites is feasible. The uppermost-Miocene gravel-bearing interval containing pebbles of volcanic rocks in Unit II, encountered at 620.9 mbsf at this site, can be seismically correlated with the gravel interval sampled at 598.5 mbsf at Site 977. This confirms not only that this gravel-bearing sedimentary interval corresponds to the "M"-reflector, but that this reflector represents a major erosional event in the Eastern Alboran Basin, possibly from the early Pliocene flooding of the Mediterranean.

Drilling at Site 978 was successful in sampling the postrift and the uppermost part of the synrift sequence of the Eastern Alboran Basin and in determining that late synrift sediments correspond to the upper Miocene (Tortonian). Post-cruise studies will help to clarify the paleodepth of deposition for this upper Miocene facies and will allow us to evaluate the rate of synrift to postrift subsidence for the Eastern Alboran Basin.

BACKGROUND AND OBJECTIVES

Site 977 Background and Objectives section was written for both Sites 977 and 978. See "Background and Objectives" section, "Site 977" chapter.

OPERATIONS

Transit Site 977 to Site 978 (Alb-4B)

After the short, 13-nmi (1.5 hr, 8.67 nmi/hr) transit to Site 978, we deployed two beacons at 1600 hr and 1840 hr, respectively, on 15 June. No site survey was performed since existing seismic data were sufficient to select the site and to correlate coring results throughout this part of the Eastern Alboran Basin. The elevation of the DES above sea level was 11.60 m for Hole 978A.

Hole 978A (Alb-4B)

We offset the ship 100 m northwest of the beacon to ensure that we were >0.5 nmi away from the known coordinates of a telecommunication cable. Hole 978A was drilled at 36°13.867'N, 2°03.424'W. The same RCB BHA was run as was used in Hole 977A, except that we added a new MBR and drill bit. To save time and reach the deep objectives as quickly as possible, the scientists requested the bit be lowered to the seafloor without using the VIT to determine the exact seafloor depth. The seafloor depth was determined to be at 1954 mbrf (1942.4 mbsl) based on the drill string weight indicator as the bit entered the seafloor. (Note: The seafloor depth was later adjusted to 1941 mbrf or 1929.4 mbsl; see below). Hole 978A was spudded at 2100 hr, 15 June.

The hole was drilled with a center bit in place to 110.3 mbsf (2064.3 mbrf) where the first RCB core was taken (Table 1; see also

Table 1. Site 978 coring summary.

Core	Date (June 1995)	Time (UTC)	Depth (mbsf)	Length cored (m)	Length recovered (m)	Recovery (%)
161-978A-						
Drilled from 0.0 to 110.3 mbsf						
1R	16	0000	110.3-119.9	9.6	0.02	0.2
Drilled from 119.9 to 168.4 mbsf						
2R	16	0315	168.4-178.0	9.6	0.02	0.2
Drilled from 178.0 to 213.0 mbsf						
3R	16	0630	213.0-222.7	9.7	1.63	16.8
4R	16	0720	222.7-232.3	9.6	7.29	75.9
5R	16	0755	232.3-236.2	3.9	3.48	89.2
6R	16	0835	236.2-245.9	9.7	8.84	91.1
7R	16	0920	245.9-255.5	9.6	8.86	92.3
8R	16	1020	255.5-265.1	9.6	8.99	93.6
9R	16	1120	265.1-274.8	9.7	8.95	92.2
10R	16	1220	274.8-284.3	9.5	8.17	86.0
11R	16	1330	284.3-293.9	9.6	6.75	70.3
12R	16	1440	293.9-303.6	9.7	9.03	93.1
13R	16	1550	303.6-313.1	9.5	8.48	89.2
14R	16	1715	313.1-322.8	9.7	9.55	98.4
15R	16	1835	322.8-332.5	9.7	8.03	82.8
16R	16	2015	332.5-342.2	9.7	7.81	80.5
17R	16	2140	342.2-351.8	9.6	9.81	102.0
18R	16	2300	351.8-361.4	9.6	9.12	95.0
19R	17	0015	361.4-371.0	9.6	9.57	99.7
20R	17	0115	371.0-380.6	9.6	9.17	95.5
21R	17	0220	380.6-390.2	9.6	8.63	89.9
22R	17	0330	390.2-399.8	9.6	9.87	103.0
23R	17	0450	399.8-409.3	9.5	9.83	103.0
24R	17	0620	409.3-418.9	9.6	9.43	98.2
25R	17	0805	418.9-428.5	9.6	9.87	103.0
26R	17	1000	428.5-438.1	9.6	9.96	104.0
27R	17	1200	438.1-447.8	9.7	9.84	101.0
28R	17	1405	447.8-457.5	9.7	9.91	102.0
29R	17	1630	457.5-467.1	9.6	9.20	95.8
30R	17	1815	467.1-476.7	9.6	7.01	73.0
31R	17	2200	476.7-486.3	9.6	9.35	97.4
32R	18	0000	486.3-495.9	9.6	9.88	103.0
33R	18	0200	495.9-505.5	9.6	9.85	102.0
34R	18	0340	505.5-515.2	9.7	9.89	102.0
35R	18	0510	515.2-524.9	9.7	8.61	88.7
36R	18	0700	524.9-534.5	9.6	9.02	93.9
37R	18	0900	534.5-544.1	9.6	9.85	102.0
38R	18	1100	544.1-553.7	9.6	9.26	96.4
39R	18	1340	553.7-563.3	9.6	9.55	99.5
40R	18	1620	563.3-572.8	9.5	9.68	102.0
41R	18	1900	572.8-582.5	9.7	9.46	97.5
42R	18	2120	582.5-592.1	9.6	7.92	82.5
43R	18	2345	592.1-601.7	9.6	8.98	93.5
44R	19	0145	601.7-611.3	9.6	5.81	60.5
45R	19	0300	611.3-620.9	9.6	0.09	0.9
46R	19	0455	620.9-630.6	9.7	0.03	0.3
47R	19	0900	630.6-640.3	9.7	4.57	47.1
48R	19	1220	640.3-649.9	9.6	8.80	91.6
49R	19	1600	649.9-659.6	9.7	9.77	101.0
50R	19	1835	659.6-669.2	9.6	8.02	83.5
51R	19	2020	669.2-678.8	9.6	2.26	23.5
52R	19	2230	678.8-688.4	9.6	2.99	31.1
53R	20	0130	688.4-698.0	9.6	5.90	61.4
Coring totals:				504.2	406.66	80.7
Drilled:				193.8		
Total:				698.0		

Note: See also detailed coring summary on the CD-ROM, back pocket, this volume.

detailed coring summary on the CD-ROM, back pocket, this volume). The hole was then advanced (without coring) from 119.9 to 168.4 mbsf where a second RCB core was attempted. Recovery in Cores 978A-1R and 2R was almost zero (0.2%). The hole was then drilled from 178.0 to 213.0 mbsf where we started continuous RCB coring. At this depth, the formation was firm enough to be recovered without being washed away. Core 5R was advanced only 3.9 m for drilling convenience; the driller then could work with a full Kelly.

RCB Cores 3R to 53R were taken from 213.0 to 698.0 mbsf (2154.0 to 2629.4 mbrf). Recovery from the interval from 213.0 to 611.3 mbsf was 364.19 m (91%). Recovery was poor in the interlayered sands and gravels. The total recovery for Hole 978A was 406.7 m (80.7%; Table 1). Coring parameters were 4-25,000 lb WOB while rotating at 50-70 rpm with 100-200 amps torque, circulating seawater at 30-50 spm with pressures ranging from 150 to 400 psi with the core barrel installed.

A bit change was required to complete the hole, so we deployed a free-fall funnel (FFF) at 0530 hr, 20 June. When pulling out of the seafloor, several attempts were required before the bit would clear the FFF without dragging the FFF up. The back-reaming buttons on the bit were apparently catching the lower lip of the FFF. We rotated the pipe approximately one-quarter turn with chain tongs on the rig floor before we saw on the VIT that the FFF had dropped off, and the pipe was then withdrawn from the FFF.

Upon clearing the FFF it was noted that the drill pipe depth was shallower (~17 m; 1937 mbrf) than first reported. After attaching a new bit, we ran it back to the seafloor and reentered the FFF, while observing with the VIT. The accurate seafloor depth was 1929.4 mbsl (1941 mbrf). All previous depths were changed to reflect this correct depth.

The FFF was entered at 1530 hr, 20 June. The drill pipe was run into the hole to 33.27 mbsf (1974.27 mbrf) where it met resistance from the formation, suggesting that we probably did not reenter the previous borehole. Several attempts were made to find the same hole by raising and lowering the drill pipe. We picked up the circulating head and attempted to wash down and hopefully locate the hole; however, the bit met with the same amount of resistance. Finally, the top drive was picked up, and we unsuccessfully attempted to find the hole by rotating and washing to 150.21 mbsf (2090.21 mbrf). After 6.5 hr of unsuccessful attempts to reenter the same hole, we decided to terminate the hole and move on to the next site. A slug of heavy mud was placed in the hole prior to pulling out. The drill pipe cleared the seafloor at 2300 hr, 20 June. The beacons were released and recovered while the drill pipe was being pulled. The bit cleared the rotary table at 0230 hr, 21 June 1995.

Hole 978A exhibited similar hydrocarbon patterns as Hole 977A. Core 978A-18R contained the maximum methane recorded for the hole of 20,710 ppm. This was accompanied by 10 ppm of C₂, 77 ppm of C₃, 9 ppm of IC₄, and 8 ppm of IC₅. Gas content began to decrease below Core 978A-25R. No gas trends were observed that were considered reason to abandon the hole.

LITHOSTRATIGRAPHY

Unit Descriptions

Site 978 is located within the Eastern Alboran Basin in a small northeast-southwest-trending sub-basin flanked to the north by the Maimonides Ridge and to the south by the Al-Mansour Seamount. A single RCB hole (Hole 978A) was drilled at this site. The uppermost section (213 m) was drilled without coring except for two spot cores (Cores 978A-1R [110.3–119.9 mbsf] and 978A-2R [168.4–178.0 mbsf]) of which all recovery (2 cm per core) was given to the paleontologists. As we did not describe samples from Cores 978A-1R and 2R, they are not included in our discussion of the lithostratigraphy (see "Biostratigraphy" section, this chapter). Continuous coring began at 213 mbsf (Core 978A-3R) and continued to 698 mbsf (Core 978A-53R). Based on composition and sedimentary structures, we have subdivided the 485-m sedimentary sequence recovered at Hole 978A into three Lithologic Units (I, II, III), and further subdivided Unit I into three subunits (Table 2; Fig. 1).

Unit I: Pleistocene to Pliocene

Hole 978A, 213.0–620.9 mbsf, Core 978A-3R, 0 cm to Section 978A-45R-CC, 0 cm.

The main lithology within Unit I is grayish olive nannofossil clay to claystone. A diverse suite of minor lithologies is present and these are listed in Table 2. The color changes for each lithology are presented in Figure 2.

Unit I is variably bioturbated with common *Planolites*, *Chondrites*, and *Zoophycos*, and less frequent halo, composite, and *Skolithos* burrows (Figs. 3, 4). Locally, burrows are partly to wholly

infilled by pyrite. Foraminifers and shell fragments are dispersed throughout the unit, with some local concentrations in burrow fills and as discrete sandy/silty beds/laminae. The latter foraminifer sandy/silty layers range in thickness up to a few centimeters, have abrupt upper and lower contacts, and are locally parallel-laminated (Fig. 5). Concentrations of dark gray, mm-sized fecal pellets are present in Cores 978A-15R through 19R and Core 978A-27R (Fig. 6).

Smear-slide data from Unit I indicate similar components but in variable proportions throughout the unit, resulting in a large range of minor lithologies, as listed in Table 2. The main components are clay-sized material and carbonate. The carbonate fraction consists predominantly of nannofossils, micrite, bioclasts, and foraminifers. The micrite component includes recrystallized nannofossils, rhombs, and irregular granular carbonate. Other terrigenous components are quartz, feldspar, mica, sedimentary and low-grade metamorphic rock fragments, and accessory minerals such as garnet and zircon. Minor amounts of organic debris (up to 5%) and diagenetic opaque minerals (up to 3%) are also present.

Downhole variations in selected components from smear-slide analyses, along with measured carbonate data are given in Figures 2 and 7. Compositional shifts shown in Figures 2 and 7, along with downhole variations in sedimentary structures, have been used to differentiate several subunits within Unit I (IA, IB, and IC; Table 2). The boundaries between subunits are somewhat gradational, hence the dashed lines in Table 2.

Subunit IA: Pleistocene to Pliocene

213.0–342.2 mbsf, Core 978A-3R, 0 cm to Section 978A-17R-1, 0 cm).

Subunit IA is characterized by the presence of slightly darker layers that alternate with the dominant lithology of olive gray (5Y 4/1) to dark greenish gray (5GY 4/1) nannofossil clay. The darker beds (Type 1) range in thickness up to 65 cm, and commonly begin with a medium-dark gray (N4) sand to silt interval above an abrupt base (Fig. 8). The basal sandy/silty intervals range in thickness up to 10 cm and often exhibit normal grading and parallel lamination. These coarser sediments pass up into bioturbated finer grained ones that make up the remainder of the dark layer (e.g., olive gray (5Y 4/1) nannofossil clay; dark greenish gray (5GY 4/1) nannofossil-rich silty clay; dark greenish gray (5GY 4/1) calcareous silty clay; grayish olive (10Y 4/2) calcareous clay). Some dark layers have abrupt basal contacts and bioturbated tops, but lack a sandy/silty basal interval (e.g., Fig. 4).

A unique semi-indurated calcareous bed (packstone) is present in Subunit IA (Fig. 9; Core 978A-8R at 60–97 cm). As determined macroscopically during core description and microscopically in smear slide and thin section, the main allochems are bioclastic debris including foraminifers and fragments of red algae, molluscs, and worm tubes?. Other minor components include fragments of echinoderms, coral, bryozoans, and siliciclastic debris. The rock has a grain-supported fabric, with microsparite matrix and rare carbonate cement within intra-allochem pores (e.g., foraminifer chambers) and as minor overgrowths on echinoderm fragments. Microborings within allochems are commonly filled with pyrite?. This packstone bed has abrupt basal and upper contacts, and shows a crude upward-fining trend from granule- to sand-sized material.

Subunit IB: Pliocene

342.2–409.3 mbsf, Core 978A-17R, 0 cm to Section 978A-24R-1, 0 cm.

Subunit IB is a fairly homogeneous transitional subunit that contains a few, poorly developed versions of the dark beds found in Subunit IA (Type 1), and those present in Subunit IC (described below).

Table 2. Unit and subunit summary for Site 978.

Unit	Series	Lithology	Sedimentary structures	Occurrence	Interval (mbsf)
IA	late Pliocene to Pleistocene	Major: Nannofossil clay Minor: Nannofossil-rich clay, nannofossil-rich silty clay, nannofossil silty clay, calcareous clay, calcareous silty clay, foraminifer sand, sandy silt, silty, sandy silty clay, nannofossil ooze, packstone	Structureless, bioturbation (<i>Planolites</i> , <i>Chondrites</i> , and <i>Zoophycos</i>), rare color banding, mottling, lamination, and graded bedding	Core 978-3R-CC, 0 cm, to Core 978A-17R-1, 0 cm	213.0–342.2
IB	late Pliocene	Major: Nannofossil clay Minor: Nannofossil silty clay, foraminifer silt to sand	Bioturbation (<i>Chondrites</i> , <i>Planolites</i> , and <i>Zoophycos</i>), rare laminations, local concentrations of shell fragments and disseminated pyrite	Core 978A-17R-1, 0 cm, to Core 978A-24R-1, 0 cm	342.2–409.3
IC	early Pliocene to late Pliocene	Major: Nannofossil claystone, calcareous claystone, calcareous silty claystone Minor: Nannofossil silty claystone, nannofossil chalk, foraminifer siltstone to sandstone, sandy silty claystone	Bioturbation (<i>Zoophycos</i> , <i>Chondrites</i> , and <i>Planolites</i>) mottling, lamination, soft-sediment deformation (slump?), local concentrations of shell fragments and disseminated pyrite	Core 978A-24R-1, 0 cm, to Core 978A-46R-1, 0 cm	409.3–620.9
II	early Pliocene to ?	Pebbles of volcanic and sedimentary rocks	None (poor recovery)	Core 978A-45R-1, 0 cm, to Core 978A-47R-1, 7 cm	620.9–630.67
III	Miocene	Calcareous siltstone, calcareous silty claystone, calcareous silty sandstone, silty claystone, claystone, clayey silty sandstone, clayey sandstone, nannofossil-rich claystone	Normal grading and upward coarsening, inverse grading, parallel lamination, cross-lamination, mottling, minor bioturbation, in situ breccia	Core 978A-47R-1, 7 cm, to Core 978A-53R-CC, 13 cm	630.67–694.3

It is characterized by rather uniform color and composition (Table 2; Figs. 2, 7), minor bioturbation, and the presence of at least one thin foraminifer silt/sand layer per core.

Subunit IC: Pliocene

409.3–620.9 mbsf, Section 978A-24R-1, 0 cm to Section 978A-46R-1, 0 cm.

The top of Subunit IC marks where the sediments are sufficiently indurated to use the suffix “stone” and the term “chalk.” Subunit IC is characterized by the presence of thick alternating dark and light beds of nannofossil claystone, calcareous claystone, nannofossil silty claystone, and calcareous silty claystone. The lighter beds are commonly greenish gray to light olive gray to dusky yellow green (5GY 5/1; 5GY 6/1; 5Y 6/1; 5Y 5/2; 5GY 5/2; 5Y 5/1), whereas the darker beds are commonly dark greenish gray to grayish olive to olive gray (5GY 4/1; 10Y 4/2; 5Y 4/1). The darker beds are progressively less calcareous and the lighter beds become progressively more rich in carbonate content (chalk) with depth (Fig. 7). The darker beds (Type 2) have common *Chondrites* burrows; sharp bases (Fig. 10) are commonly obscured by bioturbation (Fig. 11), are gradational, and have bioturbated upper contacts (Fig. 12). The lighter, more intensely bioturbated intervals have abundant *Planolites* burrows. The major compositional distinction between light and dark intervals is the proportion of nannofossils: the lighter layers commonly contain 15% more than darker intervals in the same core, hence the somewhat bimodal distribution of carbonate and nannofossil content in Subunit IC (Fig. 7).

The downhole occurrences of dark beds with sharp basal contacts (Type 1, Subunit IA) vs. those with gradational- or bioturbated-basal contacts (Type 2, Subunit IC) is summarized in Figure 13. The thickness distribution of these intervals is shown in Figure 14, and the downhole variation in thickness is pictured in Figure 15. In general, Type 1 beds are more common in the upper 200 m of Unit I, whereas Type 2 beds are prevalent in the lower 200 m of Unit I. The frequency

of these intervals can be calculated using the sediment accumulation rates presented in the “Biostratigraphy” section, this chapter. The sediment accumulation rate for the interval 223.03–375.57 mbsf, a zone with 114 Type 1 beds, is 143 m/m.y., whereas the sediment accumulation rate for the interval 398.69–570.2 mbsf, a zone with 87 Type 2 beds, is 93 m/m.y. The calculated recurrence interval for the Type 1 beds is 9357 yr, whereas the recurrence interval for the Type 2 beds is 20,116 yr.

An interval of laminated nannofossil chalk exhibits soft-sediment folding (slump?) from Sample 978A-43R-4, 39 cm to 43R-5, 110 cm. The folded sediment is crosscut by burrows (Fig. 16). The base of the slump is marked by a shear zone where darker burrow fills have been smeared out; this interval is also associated with dewatering veinlets (Fig. 17). A silty clay layer directly overlying the slumped interval (Core 978A-43R-4, at 23–26.5 cm; Fig. 18) contains approximately 15% zeolite minerals and relict microlitic textures in grains, suggesting that it may be an altered tuff.

Unit II: Lower Pliocene to Upper Miocene

Hole 978A, 620.9–630.67 mbsf, Section 978A-46R-CC, 0 cm to Section 978A-47R-1, 7 cm).

Unit II constitutes a gravel-bearing, low-recovery interval. The contact between Units I and II was not recovered. The lithologies present in the short interval recovered in Core 978A-45R are similar to those found in Unit I (calcareous chalk and nannofossil silty claystone). Because of low recovery (0.9%) in this interval (611.3–620.9 mbsf) and the resultant uncertainty as to the position of the recovered material within the cored interval, the top of Unit II is placed just above the first occurrence of gravel at 0 cm in Section 978A-46R-CC. The base of this unit is placed in Core 978A-47R, at 7 cm, just below the lowermost interval containing loose pebbles, and above a severely disrupted zone with fragments similar to underlying coherent lithologies of Unit III. (Note that some pebbles were lodged along the liner in this disrupted zone and they were placed in the uppermost

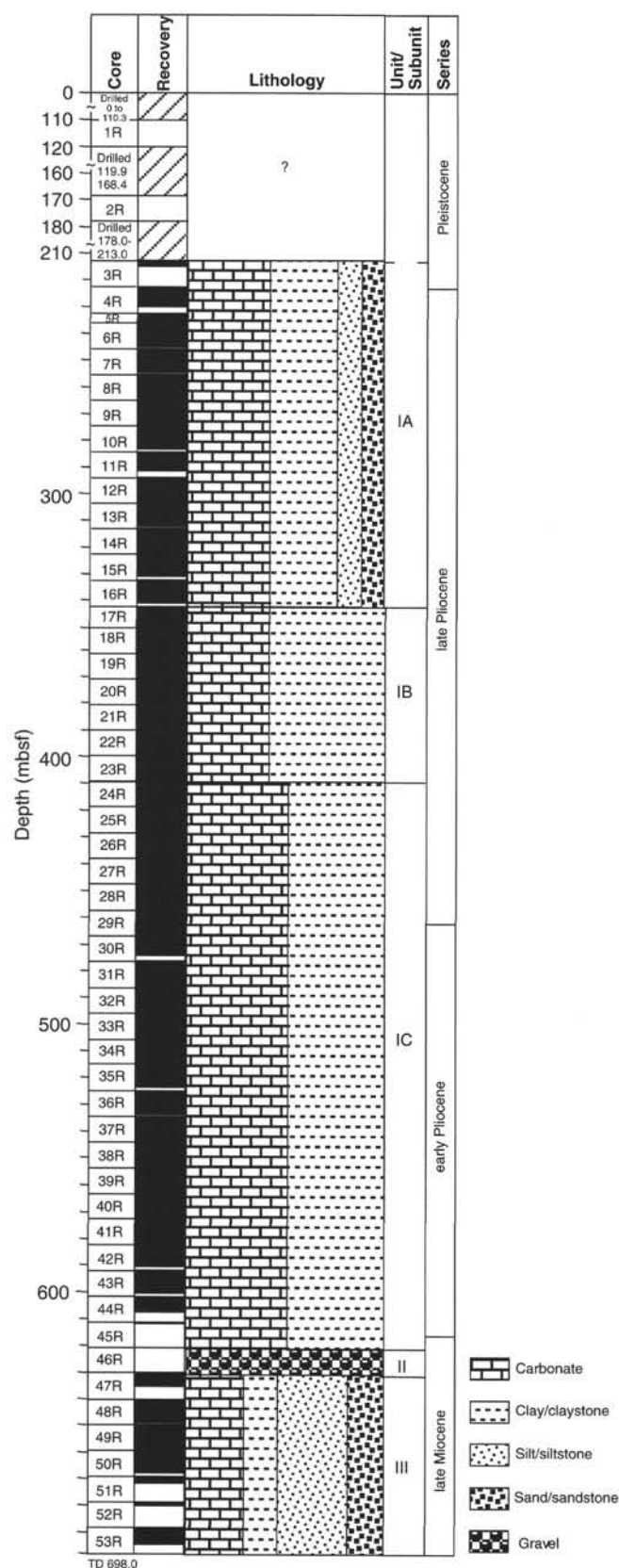


Figure 1. Simplified stratigraphic column for Site 978.

pebble-rich interval.) The ODP convention of sliding recovered intervals to the top of the cored interval, coupled with the moderate recovery in Core 978A-47R (47.1%), implies that the lower contact could be a few meters lower within the cored interval. Therefore, the total thickness of the gravel-bearing interval (Unit II) may be greater than 10.23 m, up to maximum of 24.97 m, with the addition of unrecovered intervals in Cores 978A-45R (9.51 m) and 47R (5.13 m).

The material recovered in Unit II consists of pebbles of volcanic and sedimentary rocks. They range in size from $14 \times 11 \times 8$ mm to $40 \times 28 \times 28$ mm, and are well-rounded to angular in shape. The total volume of material recovered is approximately 143 cm^3 , with three pebbles recovered in Section 978A-46R-1 and 96 pebbles recovered in Section 978A-47R-1. Some pebbles have smooth, rounded, weathered surfaces and some are partly covered by a thin coating of microcrystalline calcareous material, zeolites, and smectite, possibly representing matrix or cement.

The pebbles were first subdivided into two groups based on initial macroscopic inspection: one group from Core 978A-46R-1 (Group 1) and the other from 978A-47R-1 (Group 2). The group from Core 978A-47R-1 was further subdivided into three subgroups (Subgroups 2a, 2b, 2c). Thin sections of representative samples from each of the groups were prepared and described in detail. The first group (Group 1) consists of three rounded to subangular pebbles with an average size of $37 \times 27 \times 21$ mm. These pebbles likely have similar composition in that they macroscopically have porphyritic texture with grayish green hypohyaline fine-grained matrix. In thin section, one specimen exhibits a spherulitic to microlitic (plagioclase, pyroxene, olivine) glass matrix containing subhedral to euhedral olivine, euhedral pyroxene (orthopyroxene, clinopyroxene), subhedral plagioclase phenocrysts. Fe-oxides are included in the matrix and in olivine phenocrysts.

Group 2 is composed of mostly subrounded to subangular (rounded 19%, subrounded 39%, subangular 27%, angular 15%) pebbles with an average size of $14 \times 11 \times 8$ mm. The pebbles can be divided (macroscopically) into three subgroups of probably similar composition. The first subgroup (2a; Fig. 19) consists of grayish light to dark olive, primarily subangular pebbles with aphanitic and porphyritic textures. In thin section, the hypocrystalline, fine-grained, microlitic (plagioclase, pyroxene) groundmass contains subhedral pyroxene (clinopyroxene), euhedral olivine, and amphibole. A patch of vitric groundmass is enriched in phenocrysts of pyroxene. Based on petrographic observations, the Subgroup 2a pebbles are likely andesitic basalt to andesite in composition. Subgroup 2b (Fig. 20) consists of grayish, mostly subrounded pebbles. Petrographic examination of one pebble from Subgroup 2b shows that it is holocrystalline and fine grained, with a seriate texture of a microlitic to spherulitic groundmass of pyroxene and plagioclase. This groundmass contains anhedral phenocrysts of orthoclase, biotite, olivine, pyroxene, amphibole, quartz, and iron oxide. The amphibole and biotite phenocrysts are partly altered to chlorite. Based on petrographic observations, the Subgroup 2b pebbles have a dacitic or trachytic composition. The third subgroup (2c; Fig. 21) consists of a diverse suite of nonvolcanic pebbles, with variable color and composition. They range from rounded to subangular and are predominantly aphanitic. Macroscopically, this group contains pebbles of chert, limestone, quartzite, and metamorphic rocks. A thin section produced from one pebble shows it to be a dolomicrosparite with possible ghosts of recrystallized allochems in a microsparite matrix.

Unit III: Miocene

Hole 978A, 630.67–694.3 mbsf, Section 978A-46R-1, 0 cm to Section 978A-53R-CC, 13 cm).

The Miocene sediments that constitute Unit III are very different from the overlying marine sequences in Unit I in terms of color, com-

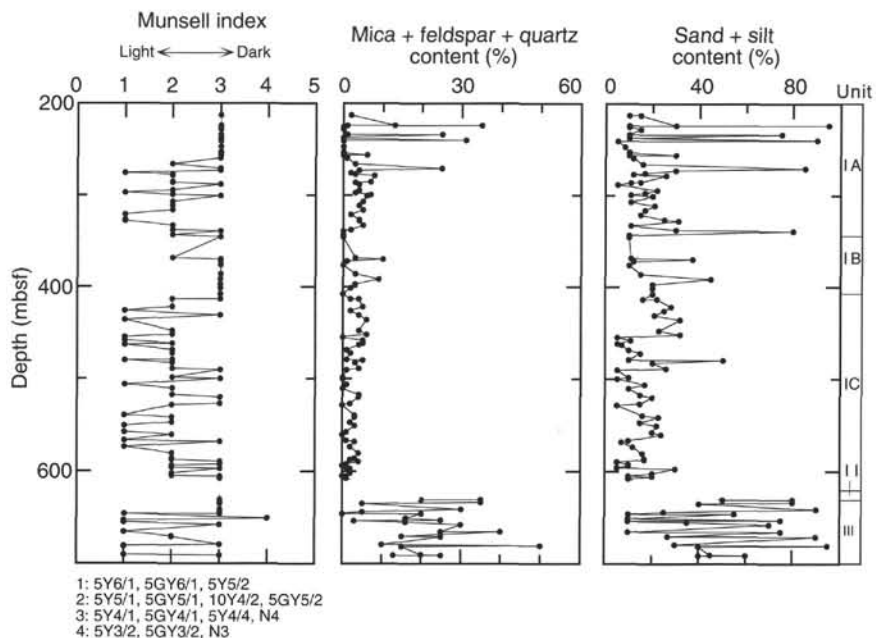


Figure 2. Graphs of Munsell color variations, and % mica + feldspar + quartz and sand + silt content at Hole 978A vs. depth.

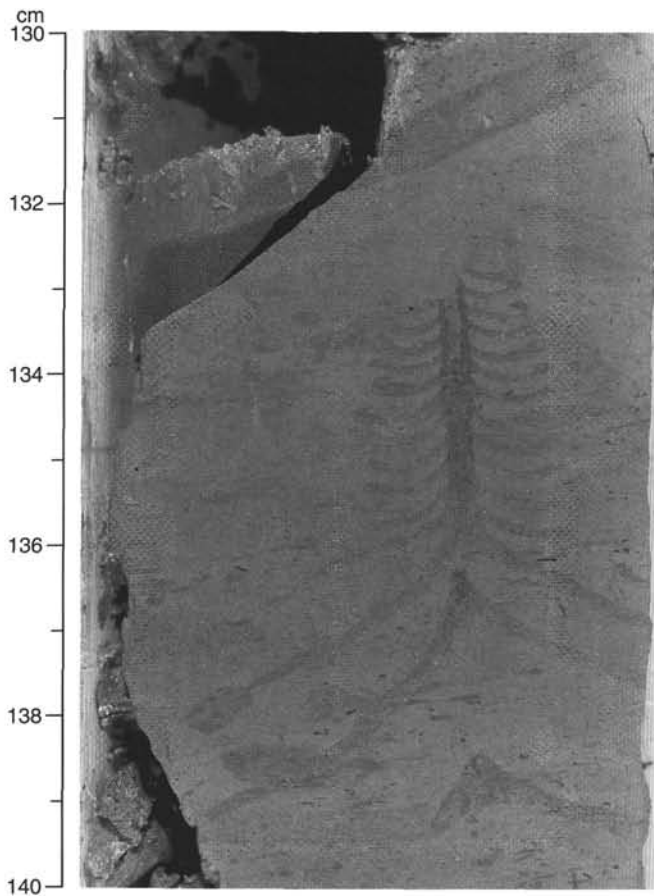


Figure 3. Tree-like *Skolithos?* burrow. Core 978A-39R-3, 130–140 cm (558.0–558.1 mbsf).

position, and sedimentary structures. The dominant lithologies are silty claystone, clayey siltstone, silty sandstone, claystone, sandy silty claystone, and clayey sandstone all with variable, but generally low (14%–32%; average = 22%) carbonate content. Colors of these lithologies range from (1) light olive-, olive- to dark-greenish gray, (2) grayish olive, to (3) moderate olive brown (5Y 4/1; 5GY 4/1; 5GY 5/2; 10Y 4/2; 5Y 3/2; 5Y 4/4). These lithologies are moderately to thinly interbedded to interlaminated. The sandy and silty sequences commonly overlie sharp basal contacts that are locally scoured (Fig. 22), and exhibit parallel and cross lamination (Figs. 22, 23), and inverse (Fig. 24) to normal grading (Fig. 25). The bases of the sandy intervals are sometimes inversely graded, but then pass up into normally graded sequences with cross-lamination, parallel lamination, and abrupt to gradational tops (Fig. 24). Very fine sub-millimeter-scale lamination similar to varves is locally present within the clay-rich intervals (Fig. 26). Types of sediment couplets observed include sandy siltstone and silty claystone; siltstone and claystone; and sandstone and siltstone. Amalgamation is very common, often resulting in decimeter sequences of sharp-based siltstone and sandstone beds. Sparse burrows are present throughout the sequence (Figs. 23, 25). Other structures present in this unit include possible dish structures, in situ brecciation (Fig. 27), boudinage, faulting (Fig. 22), and clastic dikes (Figs. 28, 29). This deformation, coupled with drilling-induced biscuiting, inhibited detailed description of some intervals.

The primary components of the sediments in Unit III are, in decreasing order of abundance, clay-sized material, micrite and inorganic carbonate, mica, quartz, nannofossils, and feldspar. The carbonate fraction exhibits a wide range of crystal morphologies, including needles, rhombs, and zoned rhombs. The mica category includes fragments of biotite, muscovite, and chlorite. Other lesser components include foraminifers, bioclasts, iron oxides, rock fragments, accessory minerals, and plant debris. Identified accessory minerals include zircon, sphene, and garnet. The rock fragments present include quartz-mica schist, chlorite schist, shale, and limestone (micritic). The iron oxides are commonly associated with clay minerals in discrete particles and as coatings on feldspar grains. Possible detrital gypsum was observed in a smear slide at 978A-47R-1, 47 cm.

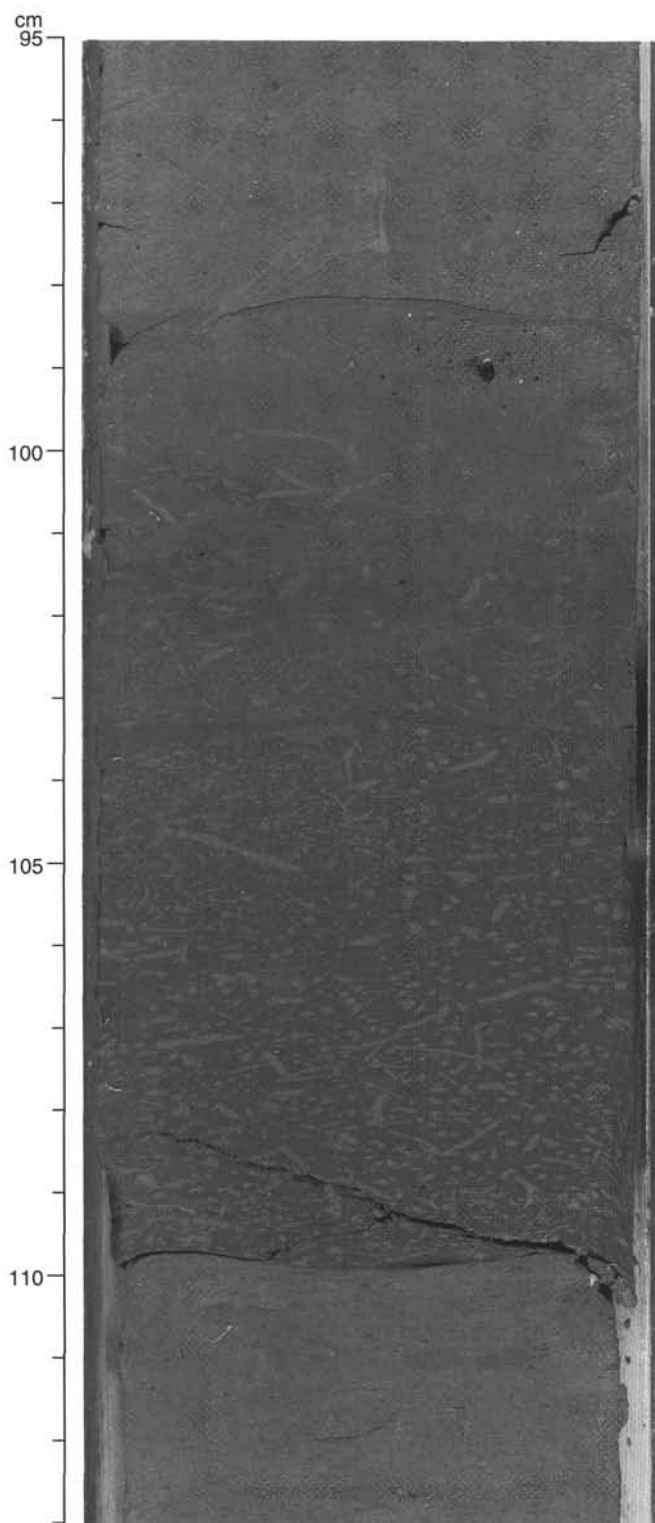


Figure 4. Sharp-based dark silty layer with abundant *Chondrites* burrows. Note biscuit margins at 98.5 and 103.5 cm. Core 978A-15R-4, 95–113 cm (328.25–328.43 mbsf).

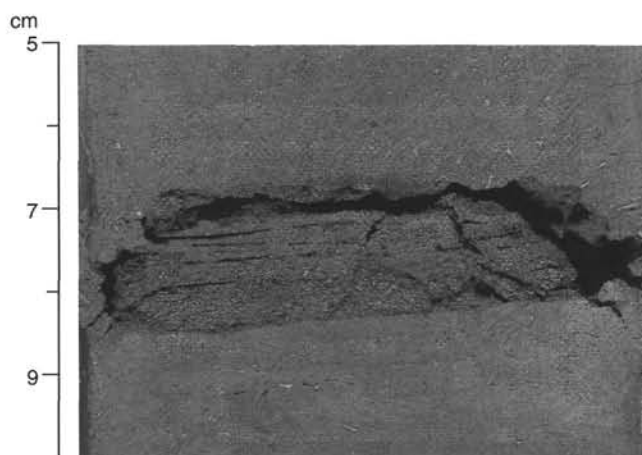


Figure 5. Dark gray (N4) laminated layer of foraminifer-rich sandy silt exhibiting abrupt lower and upper contacts. Core 978A-9R-3, 6–10 cm (268.16–268.2 mbsf).

Interpretation of Sediments Recovered at Site 978

Unit I

The pelagic to hemipelagic sediments of Unit I contain calcareous nannofossil and foraminifer assemblages that are consistent with open marine conditions and deposition in upper mesobathyal to lower mesobathyal depths (1000–4000 m), above the carbonate compensation depth (CCD), with common reworking from shallower depths (see “Biostratigraphy” section, this chapter). Ichnofacies present in Unit I sediments (e.g., *Chondrites*, *Zoophycos*, and *Planolites*) also support deposition in this depth range. There is some variation in carbonate content among subunits of Unit I, particularly a tendency towards bimodality in Subunit IC, associated with alternating dark (less carbonate; ≈40%) and light (more carbonate; ≈55%) layers. As discussed below, this bimodality may be linked to climatic variations.

The thin, laminated foraminifer and bioclastic sandy/silty layers that occur throughout Unit I are probably the product of winnowing by contour currents. Supporting evidence for this interpretation comes from their uniform thickness (commonly 1–2 cm), their abrupt basal and upper contacts, their composition (mostly foraminifers and bioclasts, commonly dispersed in underlying lithologies), and the presence of parallel lamination. Verification of this interpretation requires more detailed work, particularly grain-size analysis.

The abrupt basal contacts of the Type 1 dark beds, in addition to their laminated to cross-laminated sandy/silty bases and bioturbated tops, are consistent with deposition by low-density turbidity currents (Pickering et al., 1989). Alternatively, given the frequent occurrence of the proposed foraminifer contourite layers in Unit I, the Type 1 dark beds could also be the product of deposition from muddy contour currents. Again, detailed grain-size analysis is needed to help differentiate the origin of these deposits.

The calculated recurrence interval of approximately 20,100 yr for Type 2 dark beds in Subunit IC suggests that their apparent cyclicity may be tied to climate change related to the precession of the Earth’s orbit during the Pliocene. The presence of moderately to intensely bioturbated tops and bottoms of these intervals implies that they represent gradual shifts in sediment composition, rather than discrete relatively instantaneous depositional “events.” The compositional variation between the light and dark beds is mostly a function of nannofossil content. In smear slides, there is no distinct difference between the proportion of terrigenous silt and sand-sized components in the dark vs. the light layers. This would suggest that perhaps the variations in nannofossil content are a function of surface-water pro-

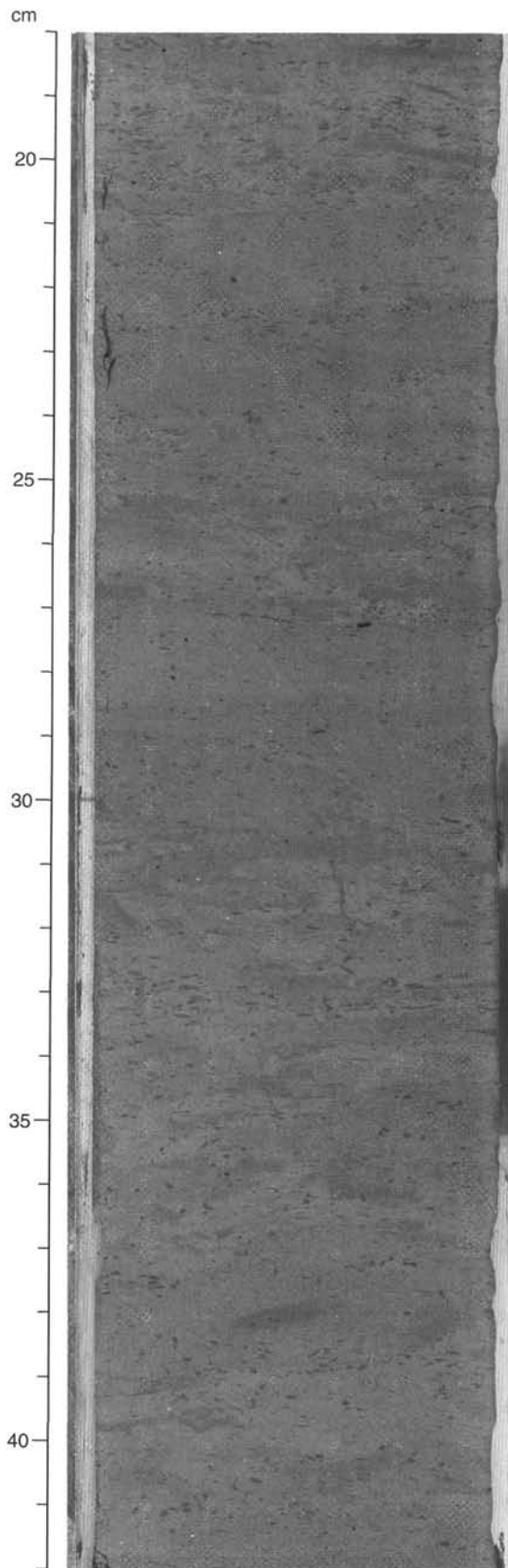


Figure 6. Intensely bioturbated nannofossil clay with common dark millimeter-sized fecal pellets. Core 978A-17R-3, 18–42 cm (345.38–345.62 mbsf).

ductivity, or alternatively, fluctuations in the local CCD. The recurrence interval of the Type 1 beds, approximately half that of the Type 2 beds, suggests that they could also be linked to climatic change. Somewhat coincidentally, the switch from dominantly Type 2 to Type 1 dark beds is located at a change in slope of the sediment accumulation curve (between 375.57 and 398.69 m; Fig. 30), at approximately 3 m.y., the time of initial glaciation in the northern hemisphere (Raymo et al., 1992).

Alternatively, the change in sedimentation style and frequency of terrigenous input to the basin could be tied to basin margin tectonism. However, given the strong correlation between climate variation and the style of sedimentation at Site 978, climatic change appears to have exerted the most control on the Pliocene sedimentary sequence at this site.

Lastly, the origin of the semi-indurated calcareous deposit (packstone) in Subunit IA (Fig. 9; Core 978A-8R at 60–97 cm), bears some discussion. The suite of shallow-water allochems in this unit suggests that it was derived from a carbonate bank or reef developed on the Maimonides Ridge or the Al-Mansour Seamount. The grain-supported fabric, abrupt basal and upper contacts, and crude upward-fining trend from granule- to sand-sized material are consistent with this unit being a high concentration debris-flow deposit.

Unit II

Volcanic rocks with compositions similar to the pebbles from Unit II (andesitic basalt to andesite, dacite, and trachyte) are known onshore to the west of Cabo de Gata near Almería, Spain and from seamounts in the Eastern Alboran Basin (volcanic Alboran Ridge). These pebbles may represent channel facies associated with a “paleo-Almería” channel (Alonso and Maldonado, 1992). The modern Almería channel presently heads in the Cabo de Gata region, and also passes near the Alboran Ridge before entering the sub-basin in which Site 978 was drilled. Hence either source is plausible for the volcanic gravel in Unit II.

Unit III

The dominance of terrigenous silt- and sand-sized material within Unit III, as well as the sedimentary structures observed, including frequent amalgamation of beds, are consistent with submarine fan lobe or apron deposits. The presence of inverse grading at the base of otherwise normally graded sandstone to siltstone intervals could be attributed to traction carpets, produced by shearing at the base of high concentration turbidity currents (Pickering et al., 1989). However, the sparse ichnofacies and varve-like lamination in some intervals may correspond to anoxic marine bottom-water conditions or, alternatively, to marginal brackish or possibly even lacustrine deposition. The calcareous nannofossil assemblages indicate open marine conditions, at least for the uppermost cores (Cores 978A-47R to 978A-50R), with poorer preservation in Cores 978A-51R to 978A-53. In contrast, the foraminiferal assemblages, usually good indicators of marine environment, are poorly preserved in Unit III, and, in the case of the planktonic foraminifers, are likely reworked. Unit III at Site 978 is similar to the Miocene sediments of Unit III at Site 974, particularly in terms of sedimentary structures and gross sediment composition (see “Lithostratigraphy” section, “Site 974” chapter, this volume, for relevant discussion of possible depositional environments).

BIOSTRATIGRAPHY

Calcareous Nannofossils: Abundance and Preservation

All samples examined from Hole 978A contain common to abundant calcareous nannofossils, except Samples 978A-49R-CC, 51R-

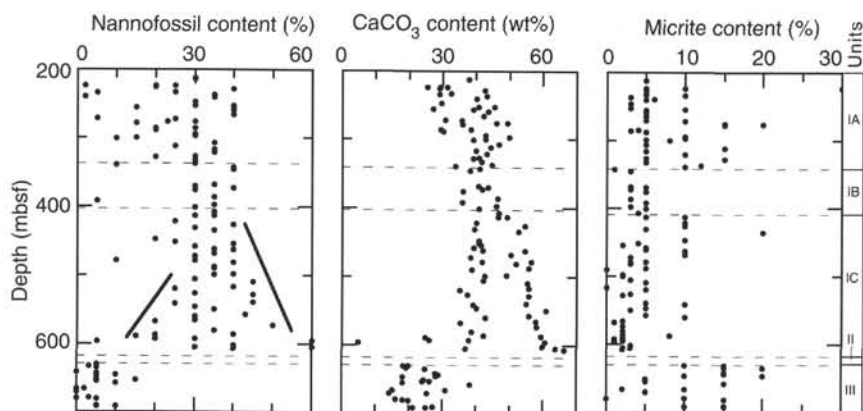


Figure 7. Graphs of % nannofossil, CaCO_3 , and micrite content at Hole 978A vs. depth. See text for discussion.

CC, 52R-CC, and 53R-CC, in which nannofossils are few. Nannofossil preservation is good in Cores 978A-1R-CC to 8R-CC; preservation is moderate or moderate to good in all other cores.

Biostratigraphy

Hole 978A (Fig. 31)

Coring was intermittent down to 213.00 mbsf, after which coring was continuous. The stratigraphic interval recovered ranges from upper Miocene (Zone NN11) to Pleistocene (Subzone NN19F). All zones and subzones in the Pliocene except Zone NN17 were identified. Because of intermittent coring, only Pleistocene Subzones NN19B, NN19D, and NN19F were found. The biozonal assignment of each core and the distribution of marker species are shown in Figure 31.

The Pliocene/Pleistocene boundary, as approximated by the first occurrence of *Gephyrocapsa oceanica*, lies between Samples 978A-4R-1, 6–8 cm (222.77 mbsf) and 4R-1, 64–66 cm (223.35 mbsf). The lower/upper Pliocene boundary lies between Samples 978A-28R-CC (457.71 mbsf) and 29R-2, 74–77 cm (459.75 mbsf).

The Miocene/Pliocene boundary occurs between Samples 978A-44R-CC (607.51 mbsf) and 978A-45R-CC (611.39 mbsf). All Miocene cores are assigned to the Rotaria Subzone (Messinian) based on the presence of *Reticulofenestra rotaria*. Also present are rare *Amorolithus delicatus* down to Core 987A-53R.

Planktonic Foraminifers: Abundance and Preservation

Planktonic foraminifers are abundant and well preserved in the Pleistocene in Hole 978A. In the Pliocene interval, foraminifers are abundant and preservation is generally good. From Samples 978A-33R-CC to 45R-CC, foraminifers show signs of enhanced dissolution or fragmentation with variable amounts of deformed or flattened tests. Miocene samples in Cores 978A-47A through 53A (641.29–694.3 mbsf) mostly yield very small (<150 μm), fragmented, or encrusted foraminifers.

Biostratigraphy

Biozones, distribution of marker species, and sampled intervals are shown in Figure 32.

Hole 978A (Fig. 32)

A lowermost Pliocene (MPL1)–Pleistocene sedimentary sequence (533 m thick) was recovered from the seafloor through 628.27 mbsf (Sample 978A-45R-CC). Below this, a 7-cm-thick gravel interval was recovered, which likely indicates an unconformity in

the sedimentary sequence. The sequence from Cores 978A-47R to 53R contain foraminifers of late Miocene age.

The Pleistocene was discontinuously cored and, therefore, it is not well documented. *Globorotalia truncatulinoides excelsa* Zone was recognized only in Sample 978A-1R-CC (110.30 mbsf) and the *Globigerina cariacensis*/*Globorotalia inflata* zonal boundary (Pliocene/Pleistocene boundary) was recognized between Samples 978A-3R-CC (214.25 mbsf) and 4R-1, 64–66 cm (223.35 mbsf).

The Pliocene is represented by all biozones (MPL6 through MPL1). *Globorotalia bononiensis* is consistently present also in Zone MPL4b. *Globorotalia margaritae* is discontinuously present in both Zones MPL3 and MPL2. Within Zone MPL3, from Sample 978A-29R-CC (466.70 mbsf) to 35R-3, 7–9 cm (518.27 mbsf), it is common only in few samples. Within Zone MPL2 *G. margaritae* was not detected from Sample 978A-39R-7, 53–55 cm (563.25 mbsf) to Sample 978A-42R-CC (590.42 mbsf). This irregular distribution of *G. margaritae* is believed to be controlled by ecologic factors. Another hypothesis explaining such an absence of *G. margaritae* could be interpreted as a repetition of the sequence caused by the common slumps in this interval. Zone MPL1 was identified from Sample 978A-44R-CC (607.28 mbsf), in which the poorly diversified assemblage characterized by *Orbulina universa*, *Globigerinoides obliquus*, *Globigerinoides extremus*, and the *Globigerina bulloides* group are abundant. This assemblage, which is commonly recorded at the very base of the Pliocene in the Mediterranean, is similar to that in MPL1 at Site 977.

Below Sample 978A-45R-CC (611.30 mbsf), planktonic foraminifers are no longer biostratigraphically reliable because they are considered reworked. However, rare specimens of *Globorotalia suterae*, *Globorotalia miotumida*, *Globorotalia cf. conomiozea* occur from Sample 978A-47R-CC (634.93 mbsf) to Sample 978A-53R-CC (694.17 mbsf) and are indicative of Messinian age. Evidence for reworking is based on the following considerations: (1) the foraminifers are a minor component of the residue, (2) they have the same size as the detrital components, and (3) the finest sediment fraction does not provide any residue or is barren in foraminifers. The assemblage recorded in these samples is similar to that recorded in the Messinian interval of Site 975.

Benthic Foraminifers

Benthic foraminifers at Site 978 (present-day water depth 1942.4 m) are larger in size, more abundant, and more diverse than at Sites 974 or 975, and are comparable in size and diversity to Sites 976 and 977. They are diagnostic of upper mesobathyal to lower mesobathyal (1000–4000 m) depths as defined by Wright (1978). They generally comprise <1%–2% of the total foraminiferal assemblage, except where there is evidence for downslope contamination by shelf taxa that are often abraded and mixed with deeper water assemblages.

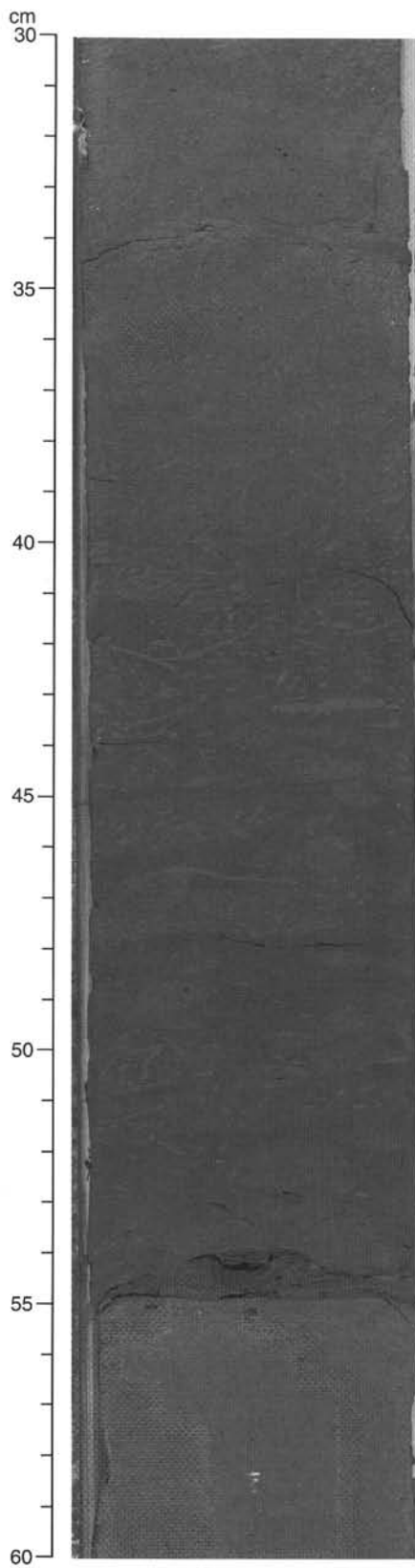


Figure 8. Dark silty interval with an abrupt lower contact (55 cm) overlain by a thin laminated bioclastic sandy/silty layer (54–55 cm) that passes up into bio-turbated nanofossil clay. Burrow types include *Planolites* and *Chondrites*. Core 978A-15R-2, 30–60 cm (324.6–324.9 mbsf).

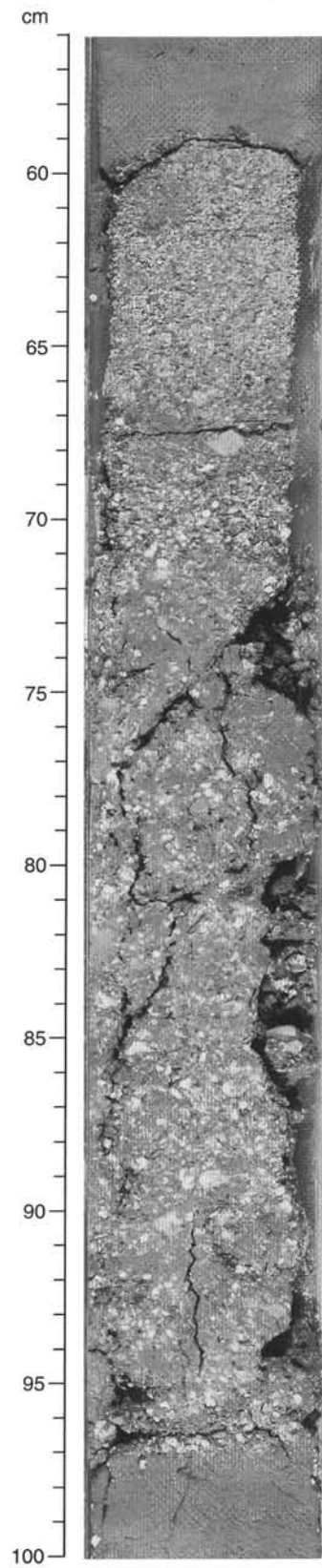


Figure 9. Packstone interval with abrupt upper and lower contacts. The matrix-rich intervals in the coarser base of the unit are probably muddy intra-clasts. The unit exhibits a crude upward-fining trend. See text for further description and discussion. Core 978A-8R-5, 56–100 cm (262.06–262.5 mbsf).

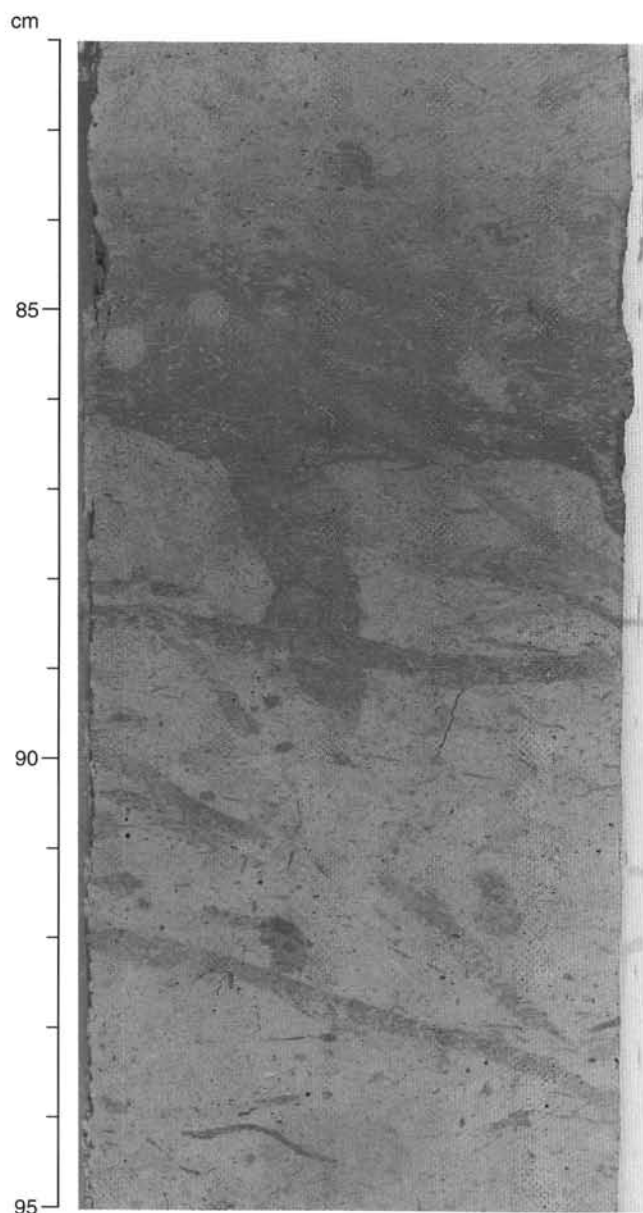


Figure 10. Bioturbated, abrupt lower contact of thin clay-rich darker interval at 83–86 cm, with common *Zoophycos* and *Chondrites*. This contact was classified as “abrupt,” making it a Type 1 dark interval. Millimeter-sized black spots are hollow foraminifer tests cut in half by the saw when the core was split. Core 978A-43R-2, 82–95 cm (594.42–594.55 mbsf).

This is more frequent at Site 978 than Site 977 and occurs in discrete intervals.

In the Miocene interval, benthic foraminifers are poorly preserved and the assemblage is not indicative of a definite environment. Rare specimens of *Brizalina dentellata* and *Bulimina echinata*, typical Mediterranean benthic species of the Messinian interval (Colalongo et al., 1979), are discontinuously present throughout the entire interval.

Biozonal Correlation

Correlation of the calcareous nannofossil and planktonic foraminiferal zonations for Hole 978A is shown in Figure 33. The placement

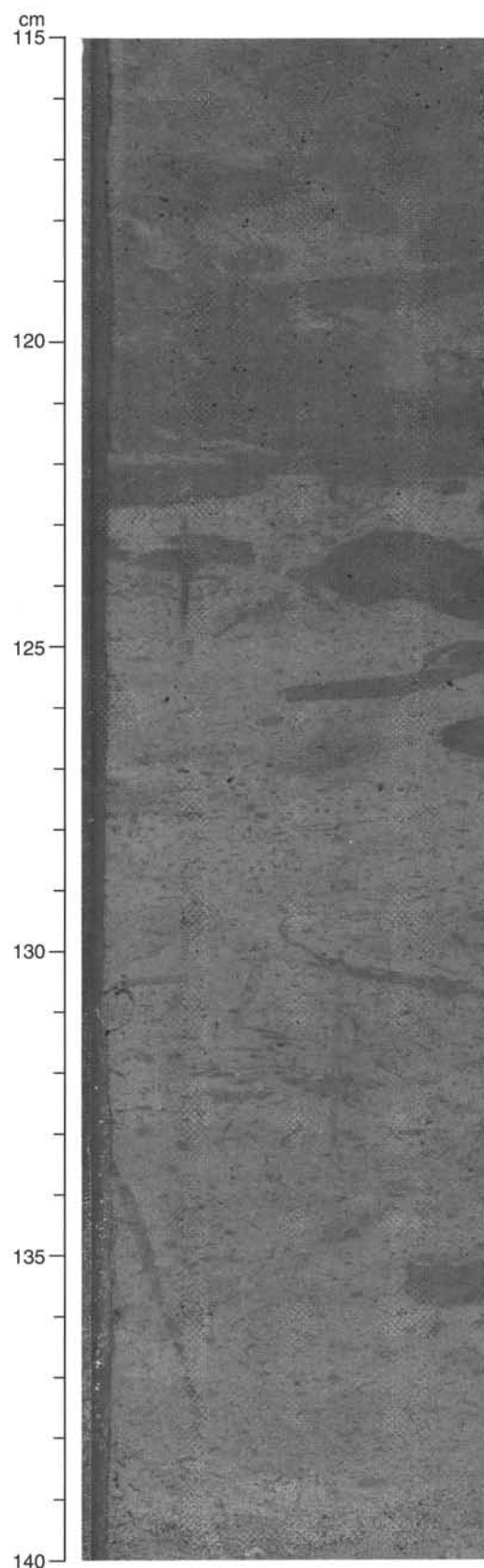


Figure 11. Bioturbated contact between a darker and lighter interval in Subunit IC. Millimeter-sized black spots are hollow foraminifer tests cut in half by the saw when the core was split. Core 978A-28R-3, 115–140 cm (451.95–452.2 mbsf).

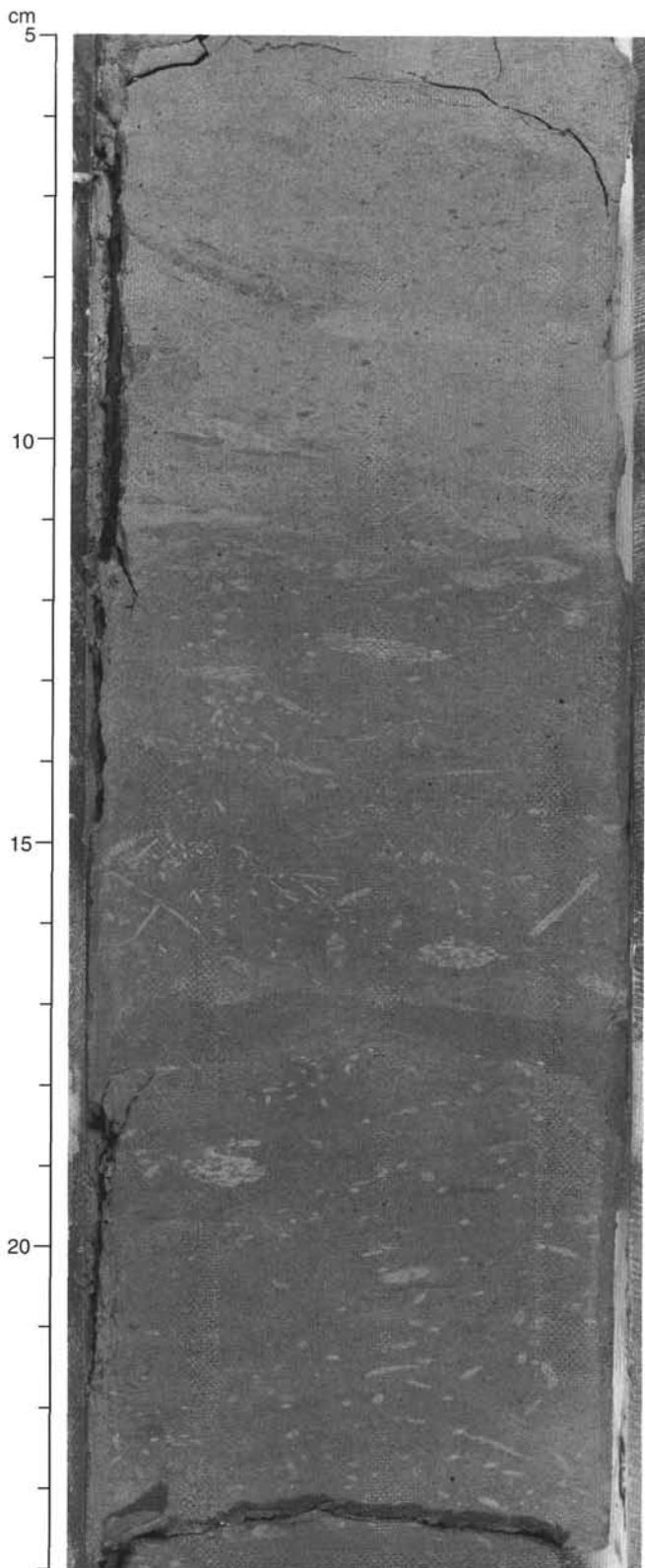


Figure 12. Bioturbated upper contact of a darker bed exhibiting *Chondrites* and composite burrows. Core 978A-36R-6, 5–24 cm (532.45–532.64 mbsf).

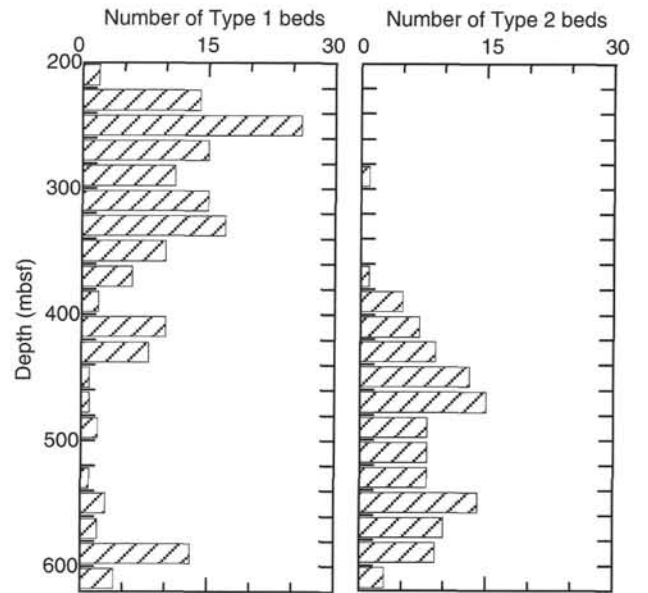


Figure 13. The downhole occurrence of dark beds with sharp basal contacts (Type 1) vs. those with gradational- or bioturbated-basal contacts (Type 2).

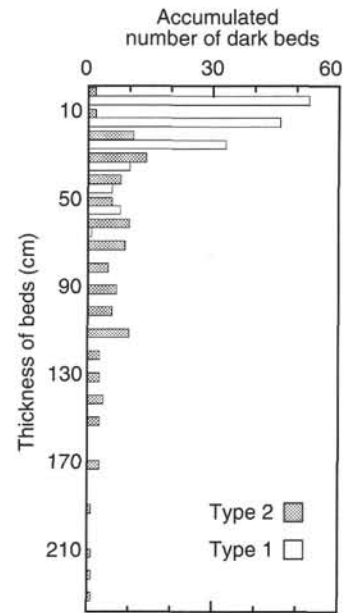


Figure 14. Thickness distribution of the Type 1 (abrupt base) and 2 (gradational- or bioturbated-base) dark beds.

of the Pliocene/Pleistocene boundary is based primarily on the calcareous nannofossils. Miocene calcareous nannofossils and planktonic foraminifers are indicative of Messinian age.

Paleoenvironment

The Pleistocene–Pliocene interval is pelagic to hemipelagic with minimally greater amounts of detrital material and displaced fauna than nearby Site 977. Planktonic and benthic foraminifers are indicative of an open-marine environment with planktonic dominant over benthic foraminifers. However, the regular presence of echinoid

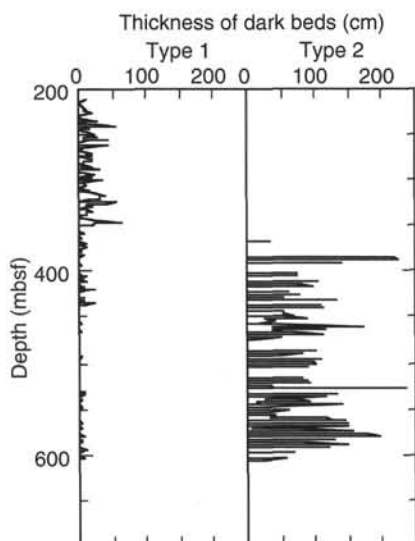


Figure 15. Downhole variation in thickness of Type 1 and Type 2 dark beds.

spines and a few inner neritic benthic foraminifers suggest weak, but continuous, sediment input from shallower waters.

The foraminiferal assemblage and associated sediment of the Miocene interval is indicative of a depositional environment close to a significant terrigenous source. Further, the detrital component is a relatively immature mixture of quartz, feldspars, and micas, the latter comprising 10%–15% of the sediment (see “Lithostratigraphy” section, this chapter). Small bathyal and a few neritic benthic foraminifers are represented. The foraminiferal assemblage shows a typical pattern of turbiditic sediments: barren samples alternate with fossiliferous ones. There are no clear indications of indigenous fauna of different size fractions. On the contrary, calcareous nannofossils indicate normal marine conditions.

Sedimentation Rates

Figure 30 shows the sedimentation rates for Hole 978A. Age data used for calculations (Table 3) are based on first and last appearance events of selected nannofossils and planktonic foraminifers, and on magnetostratigraphic chrons. Average sedimentation rates in Hole 978A were 127 m/m.y. for the Pleistocene, 111 m/m.y. for the upper Pliocene, 120 m/m.y. for the lower Pliocene, and 156 m/m.y. for the upper Miocene.

PALEOMAGNETISM

Fifty RCB cores were measured with the cryogenic magnetometer. Blanket AF demagnetization was routinely applied at 15 mT. We could identify several geomagnetic polarity zones in the interval between 390 and 610 mbsf.

Remanent Magnetization

Declination, inclination, and intensity before and after AF demagnetization are shown in Figures 34 and 35 together with low-field magnetic susceptibility (K) measured on the MST. From 210 to 440 mbsf intensities (15 mT) and K are as weak as 10^{-4} A/m and 10^{-4} SI, respectively (Fig. 35). Below 440 mbsf a sharp increase is observed, up to intensities of about 10^{-2} A/m and up to susceptibilities of about

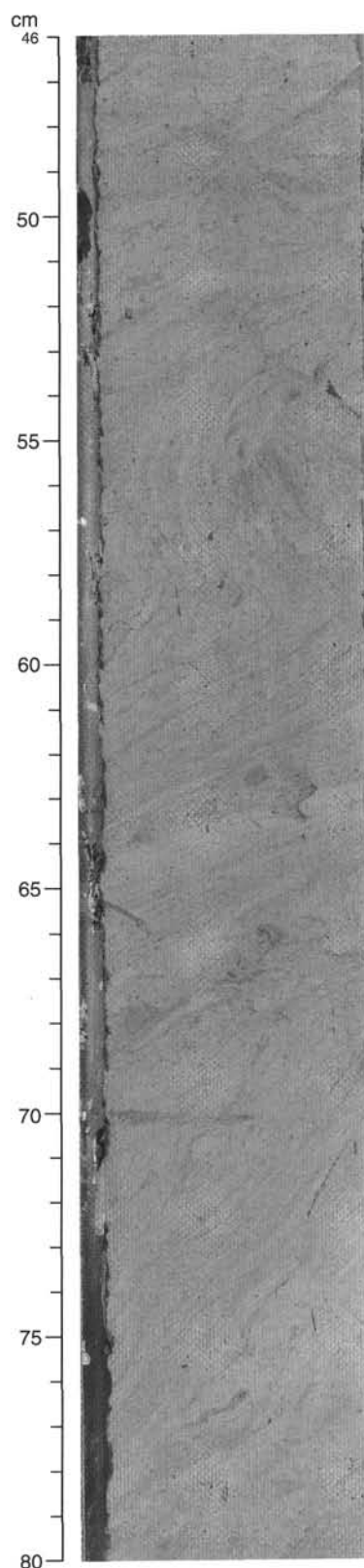


Figure 16. Soft sediment slump folding of laminated nannofossil chalk near the top of a slumped interval in Subunit IC. The apparent laminations may be stretched darker burrow fills. Upper fold limb at 52–55 cm is crosscut by burrow traces. Core 978A-43R-4, 46–80 cm (597.06–597.4 mbsf).

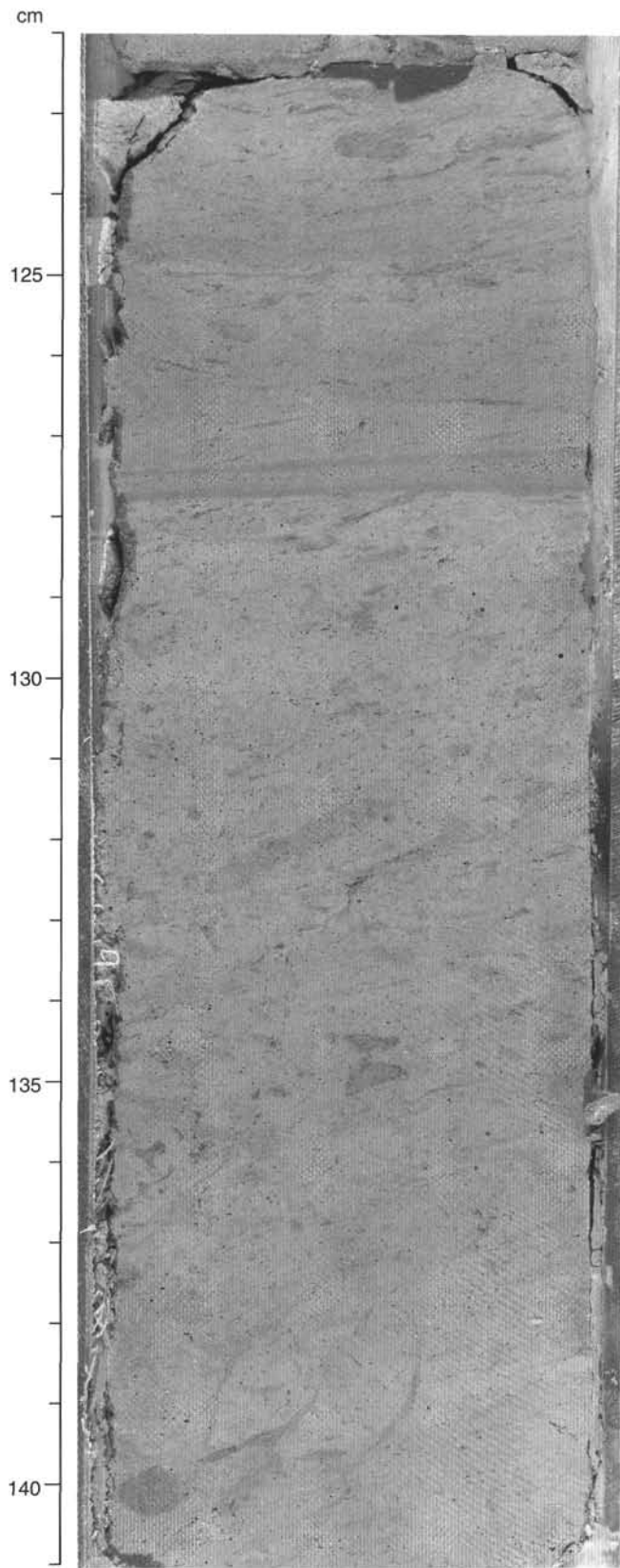


Figure 17. Shear zone near base of slump pictured in Figure 16. Dark streaks at 125–127 cm may be sheared burrow fills. Note that this interval is also associated with faint dewatering veinlets at 137–140 cm. Core 978A-43R-6, 122–141 cm (600.82–601.01 mbsf).

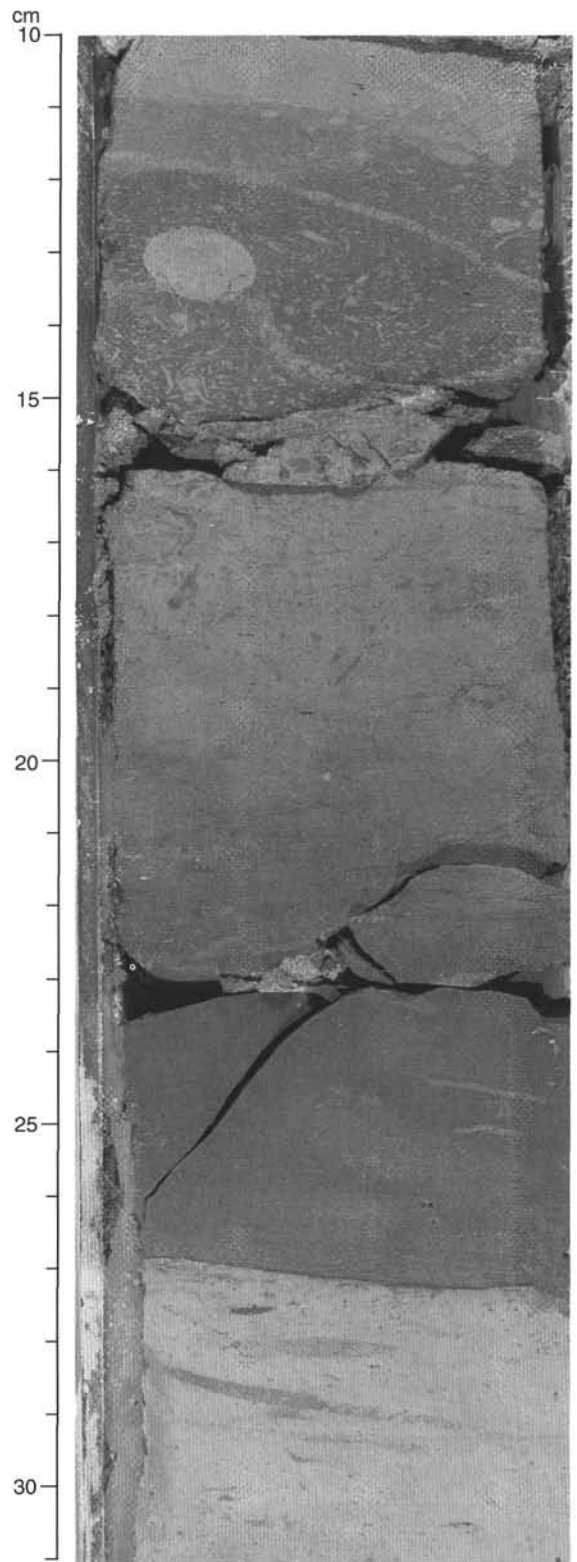


Figure 18. Silty clay layer (23–26.5 cm) above the slumped interval pictured in Figure 16. Smear-slide analysis shows that it is likely an altered tuff, because it contains approximately 15% zeolite minerals and relict microlitic volcanic textures in some grains. The upward change in color from 23 to 16 cm probably reflects pelagic input followed by deposition of a darker (bioturbated) terrigenous layer (Type 1 dark layer[?] base is biscuited). Core 978A-43R-4, 10–31 cm.

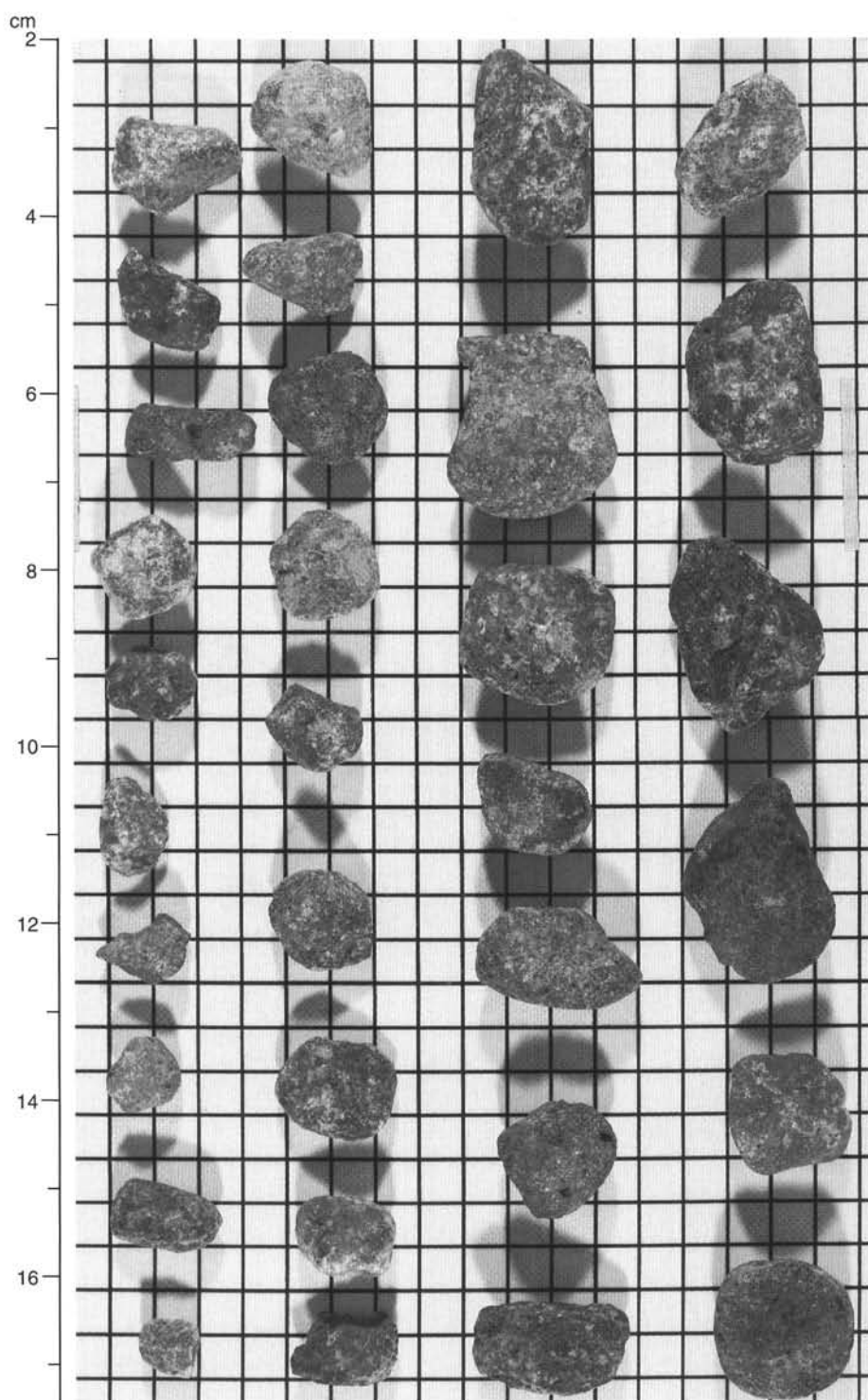


Figure 19. Close-up photograph of volcanic pebbles from Subgroup 2a. Grid spacing is 0.5 cm.

2×10^{-4} SI. From 630 to 700 mbsf, K rises again but the intensity shows little change.

Declinations are considerably scattered before demagnetization with very slight clustering around 0° below 390 mbsf, implying a weak radial overprint (Fig. 34). After AF demagnetization at 15 mT, declinations are equally scattered below 390 mbsf (Fig. 35). Above this, declinations cluster around 200° .

Before demagnetization inclinations are almost entirely positive. Application of AF of 15 mT significantly changes inclinations be-

tween 390 and 610 mbsf (Fig. 35). We can identify at least 11 polarity zones based on systematic change in inclinations as shown in Figure 36. Shallow and scattered inclinations between each polarity zone may indicate a transitional geomagnetic field or, more likely, insufficient removal of the positive overprint. Intervals from 210 to 390 mbsf and 630 to 700 mbsf are still dominated by positive inclinations.

We find that the change in inclination record does not correspond with the significant change in intensity or susceptibility at this site. The termination of the zone with well-defined polarity (390 mbsf) oc-

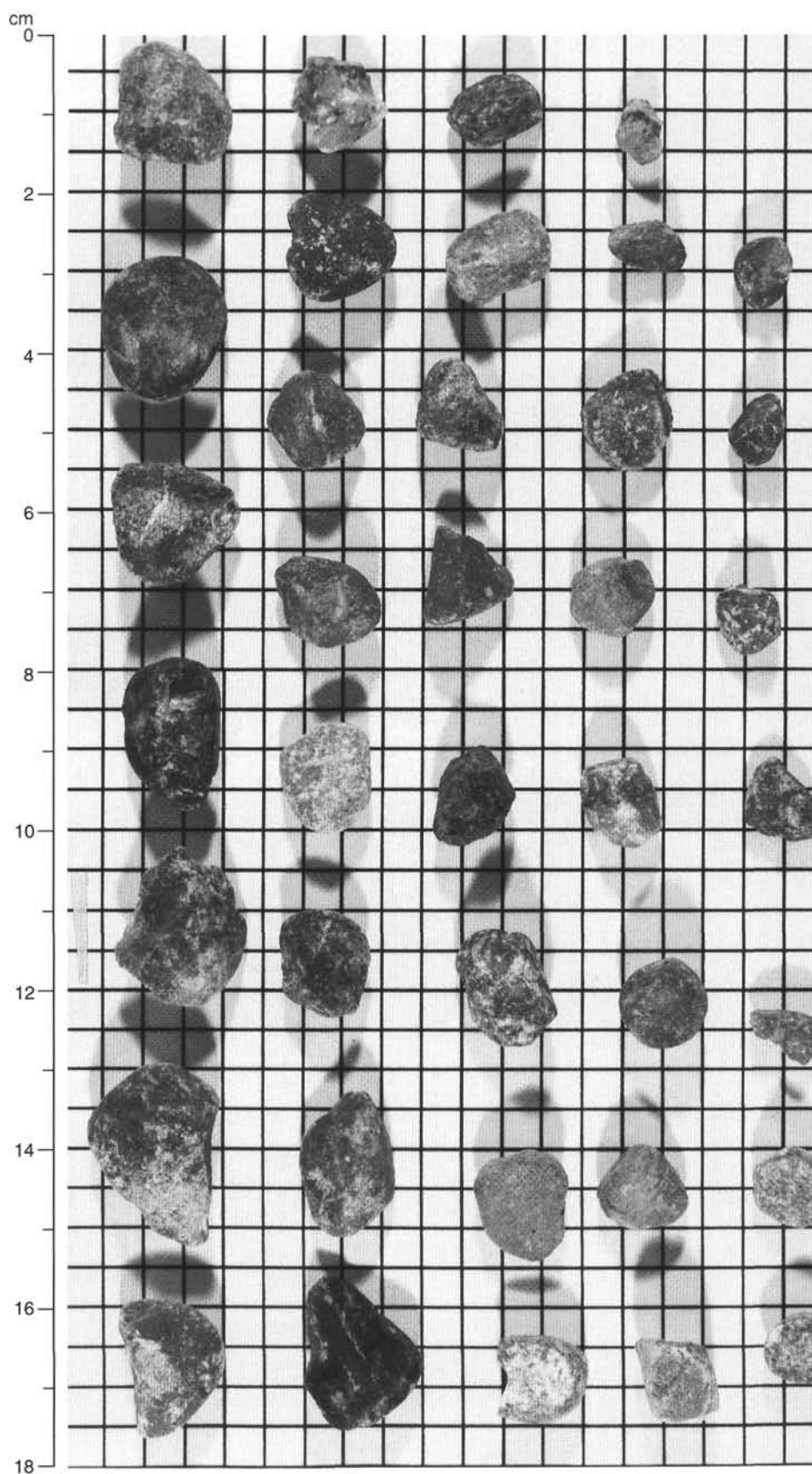


Figure 20. Close-up photograph of volcanic pebbles from Subgroup 2b. Grid spacing is 0.5 cm.

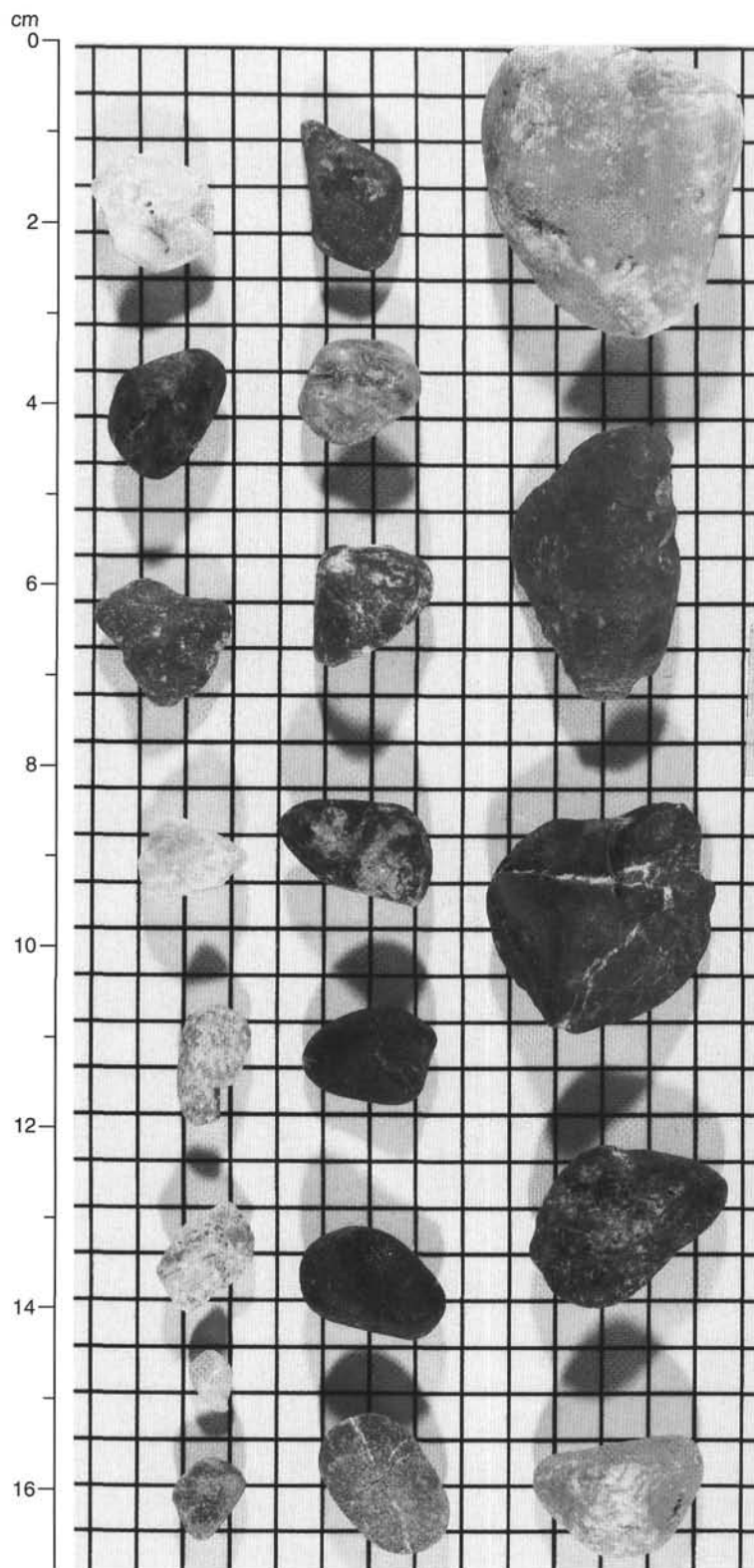


Figure 21. Close-up photograph of nonvolcanic pebbles from Subgroup 2c. Grid spacing is 0.5 cm.

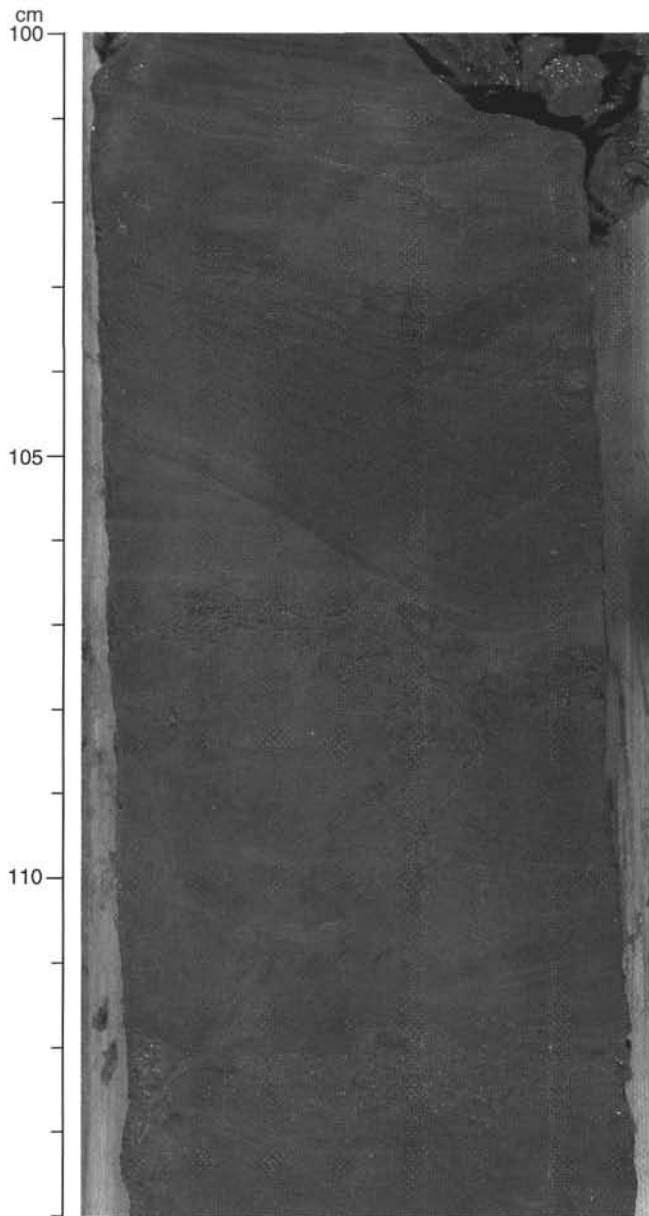


Figure 22. Scoured base of fine sandstone layer truncates laminated silty claystone at 104–107 cm. Small-scale ripple cross laminations are present from 100 to 101 cm. The sequence is probably crosscut by a reverse fault that extends from the lower left corner of the photograph at 112.5 cm up to the right of the core at 107 cm. The fault places older silty claystone on the left, adjacent to younger (repeated) fine sandstone on the right. Core 978A-53R-4, 100–114 cm (693.9–694.04 mbsf).

curs at a much shallower depth than the sharp change in intensity and K (440 mbsf). Change in *P*-wave velocity, porosity, and lithology corresponds with this significant change in inclination attitude. *P*-wave velocities indicate stepwise increase at 390 mbsf from 1.73 to 1.78 km/s (see “Physical Properties” section, this chapter). These changes may indicate an increase in consolidation and may control degree of sediment deformation during coring. Lithostratigraphic Unit IC almost coincides with this interval.

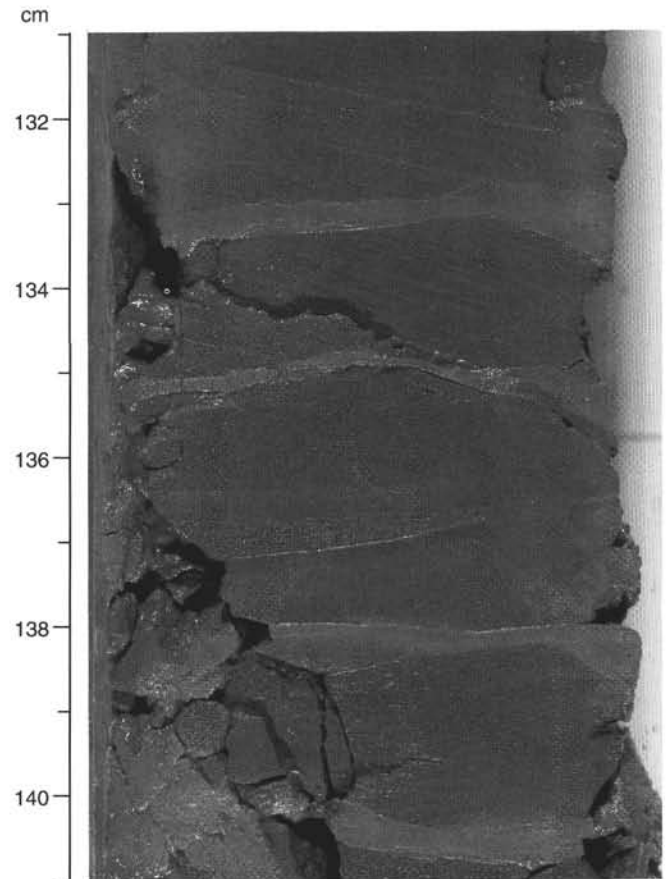


Figure 23. Cross-laminated fine sandstone from 131 to 135 cm, overlying complexly bedded/laminated interval at 135–138 cm. Note that thin dark, silty claystone laminae at 137 cm are crosscut by the faint oval burrow on the right. Core 978A-52R-1, 131–141 cm (679.11–680.21 mbsf).

The sharp increase in intensity and K was also observed at Site 977 at 420 mbsf, suggesting good correlation between two neighboring sites. Remanent directions, however, are quite different between Sites 977 and 978. This also suggests that the magnetic mineralogy change (abundance and mineral assemblage) is not the only factor controlling the reliability of paleomagnetic data. Substantial differences between these two sites may be due to coring methods used (XCB at Site 977 and RCB at Site 978). Although recovered by using RCB, the cores were less deformed and less biscuited in Lithostratigraphic Unit IC at this site. The influence of coring methods on core magnetism needs to be studied carefully.

Magnetostratigraphy

Eleven polarity zones are identified between 390 and 610 mbsf (Fig. 36). There is still some ambiguity (gray zones in Fig. 36), possibly indicating insufficient demagnetization. Several age-diagnostic microfossils were found in this interval; first common occurrence of *G. margaritae* (606 mbsf), first occurrence of *P. lacunosa* (505 mbsf), last common occurrence of *G. margaritae* (466 mbsf), and last occurrence of *G. puncticulata* (436 mbsf; see “Biostratigraphy” section, this chapter). Correlation of the biostratigraphic data and the polarity zones indicate they are mostly subchrons in Chron 3n. Correlation of polarity zones with the geomagnetic polarity time

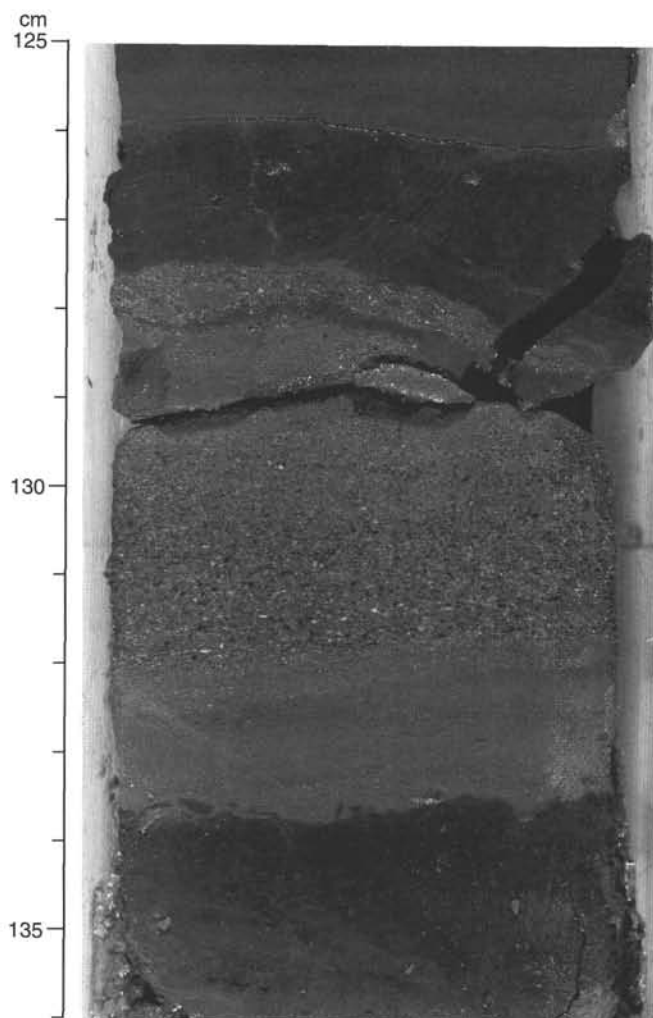


Figure 24. Silty claystone at 135 cm is overlain at a scoured contact by sandy silty claystone with clay rip-up clasts at 133 cm, that passes up into normally graded sandstone. This is an example of a unit with poorly developed basal inverse grading. Upper contact of sandstone with overlying silty claystone appears to have been modified by soft-sediment deformation. Note abrupt contact of silty claystone and dark siltstone at 126 cm. Core 978A-53R-2, 125–136 cm (691.15–691.26 mbsf).

scale (GPTS: Cande and Kent, 1995) is shown in Figure 36. Depth of chron and/or subchron boundaries based on this correlation are given in Table 4.

STRUCTURAL GEOLOGY

Site 978 is located between Al-Mansour Seamount and the Maimonides Ridge in the Eastern Alboran Basin, in an east-northeast–to west-southwest–trending trough about 15 km wide. The basin has a pre-Pliocene fill that shows evidence of tilting and internal unconformities, overlain by flat-lying Pliocene to Pleistocene sediments. This lack of deformation is reflected in the Pliocene to Pleistocene cores from Site 978. The bedding is for the most part horizontal, with local variations in dip that probably result from slump folding. An open 10-cm east-vergent slump fold is well preserved near the base of the

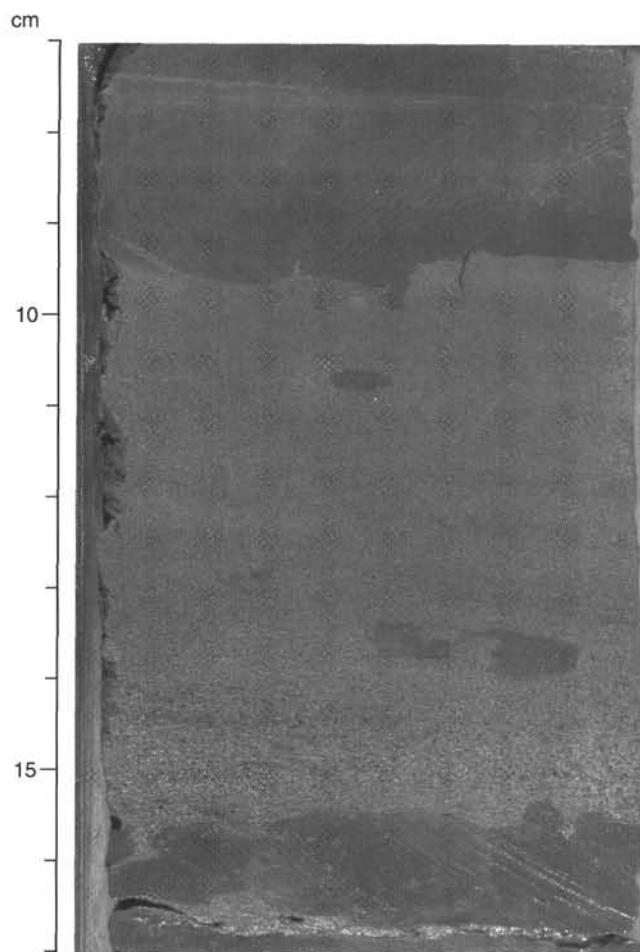


Figure 25. A bed consisting of normally graded sandstone to laminated siltstone with irregular but abrupt upper and lower contacts with adjacent silty claystone. Dark silty claystone patches within lighter graded interval may be trace fossils or, alternatively, rip-up clasts. Core 978A-53R-4, 7–17 cm (692.97–693.07 mbsf).

Pliocene in Section 978A-43R-4 (597.1 mbsf). This fold is cut by burrows, demonstrating that it formed not far below the sediment-water interface (Fig. 16). Just below, the clay has been deformed by the slumping, and the burrows have been sheared with respect to bedding and stretched (Fig. 17). There are also a few normal faults with displacement on the order of 1 cm (Fig. 37).

The late Miocene rocks below the zone of low recovery in Cores 978A-45R through 47R are significantly more lithified than the Pliocene to Pleistocene sequence, and show some remarkable deformational features. Although the bedding is horizontal, the rocks are cut by numerous dilational fractures (Fig. 38). These have very irregular orientations, but are generally at a high angle to the bedding. They vary considerably in width, branch, and form networks (Fig. 39). They are filled by pale green or gray clay, and by numerous angular fragments of the surrounding consolidated mudstone. Locally, the fracturing is so intense that the rock has been turned into an intraformational breccia (Fig. 27). The clay filling the fractures resembles the surrounding rock except that it appears to be less consolidated. In places the mud fill can be traced from a fracture to a bedding-parallel layer of the same material. A possible explanation

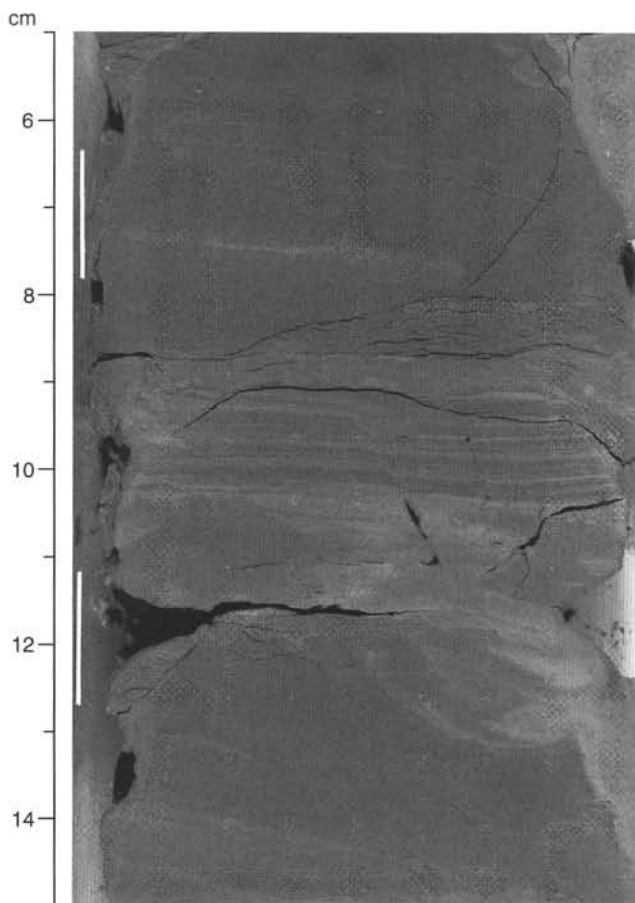


Figure 26. Finely laminated (cm- to mm- to sub-mm scale) to thinly bedded silty claystone. Small oval burrows are present at 5.5 cm and 13.5 cm. Core 978A-49R-7, 5–15 cm (658.98–659.01 mbsf).

for these features is that they are hydraulic fractures formed in consolidated clay by overpressured and underconsolidated horizons within the sequence. They are present down to the bottom of the hole.

ORGANIC GEOCHEMISTRY

Calcium carbonate and organic carbon concentrations were measured on samples obtained regularly from Hole 978A. Organic matter atomic C/N ratios and Rock-Eval analyses were employed to determine the type of organic matter contained within the sediments. Elevated amounts of headspace gases were encountered, and routine monitoring of these gases was done for drilling safety.

Inorganic and Organic Carbon Concentrations

Concentrations of carbonate carbon vary between 1.3% to 8.0% in sediments from Site 978 (Table 5; Fig. 40). These carbonate carbon concentrations are equivalent to 11% to 66% sedimentary CaCO_3 , assuming that all of the carbonate is present as pure calcite. The Miocene sediments in the lowermost lithologic unit are distinctly lower in carbonate contents (Fig. 40). The range in carbonate content reflects varying combinations of fluctuating biological productivity, dilution by non-carbonate sedimentary components, and post-depositional carbonate dissolution driven by oxidation of organic carbon during Miocene to Pleistocene times.

Sediments at Site 978 average 0.3% TOC, which is the same as the ocean-drilling average compiled by McIver (1975) from DSDP

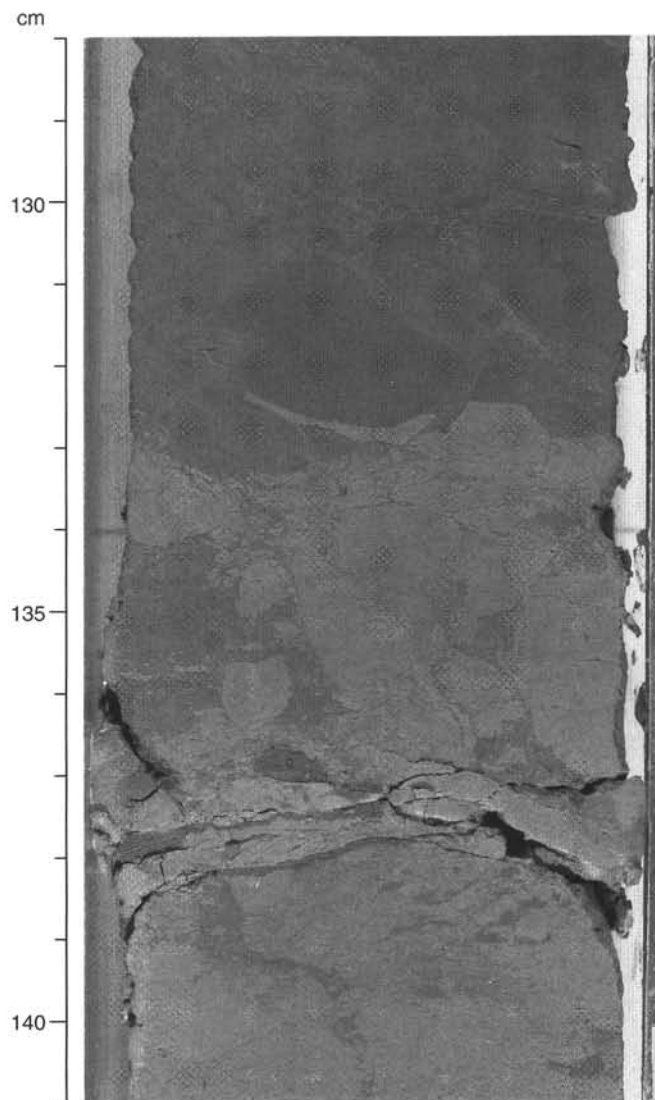


Figure 27. In situ brecciation in upper late Miocene claystone to silty claystone. The fragments all appear to be locally derived by hydraulic fracturing. Core 978A-49R-3, 128–141 cm (654.18–654.3 mbsf).

Legs 1 through 33. TOC concentrations fluctuate between 0% and 1.27% (Table 5; Fig. 40). Some of the Pleistocene sediments in which TOC concentrations are elevated resemble those referred to as sapropels at Sites 974 and 975. As such, their occurrence at Site 978 confirms the westward extension of Mediterranean sapropel deposition discovered at Site 977 (see “Site 977” chapter, “Lithostratigraphy” section, this volume).

Organic Matter Source Characterization

Organic C/N ratios were calculated for Site 978 samples using TOC and total nitrogen concentrations to help identify the origin of their organic matter. Site 978 C/N ratios vary from <5 to 45 (Table 5); most values are between 4 and 8, which is diagnostic of marine organic matter (e.g., Emerson and Hedges, 1988; Meyers, 1994).

Sediment samples having relatively elevated TOC concentrations (>0.5%) were selected for Rock-Eval characterization of the type and thermal maturity of their organic matter contents (Table 6). A van Krevelen-type plot of the hydrogen index (HI) and oxygen index (OI) values suggests that the sediments contain mostly Type III (land-de-

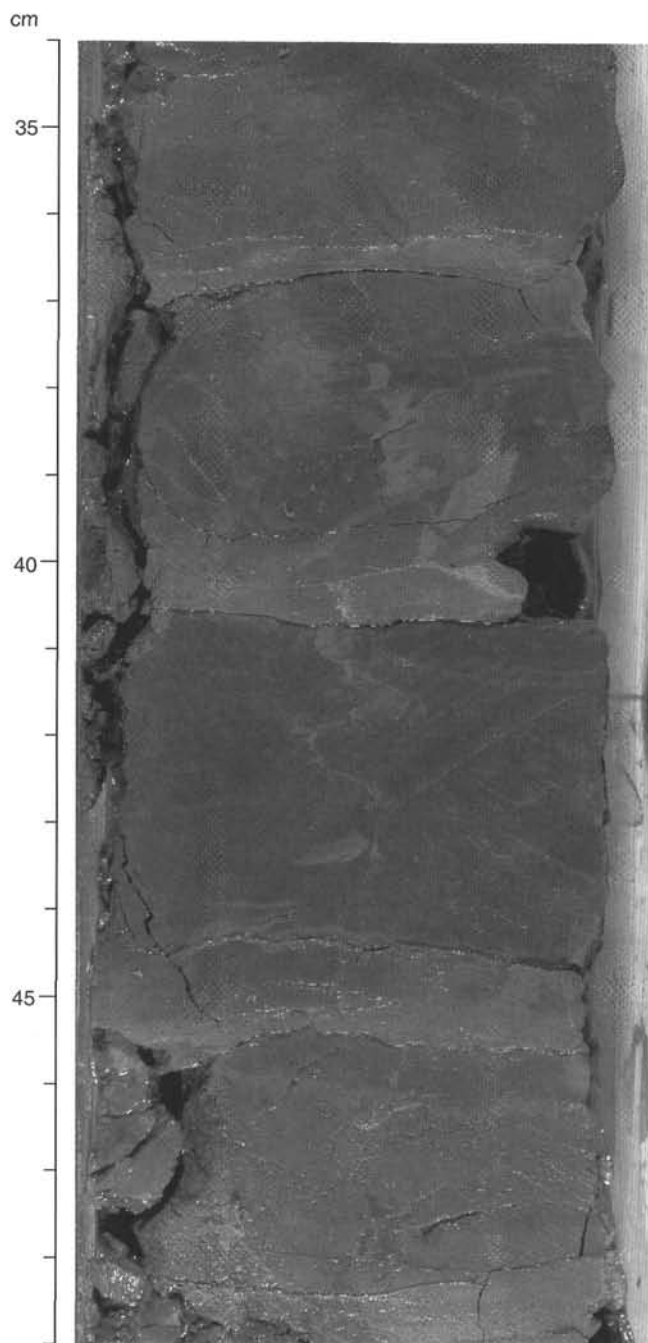


Figure 28. Example of fine clastic dikes with crosscutting relationships, particularly in the interval 37–40 cm. Core 978A-53R-2, 34–49 cm (690.24–690.39 mbsf).

rived) organic matter (Fig. 41). This source assignment for the organic matter conflicts, however, with the marine-type C/N ratios for these samples. The contradiction between the Rock-Eval source characterization and the elemental source characterization is evidence that the marine organic matter has been heavily oxidized, probably by microbial reworking. Well-preserved Type II organic matter has high HI values (Espitalié et al., 1977).

Headspace Gases

Concentrations of headspace methane are relatively high in sediments from Hole 978A (Fig. 42). Two sources of the gas are possible.

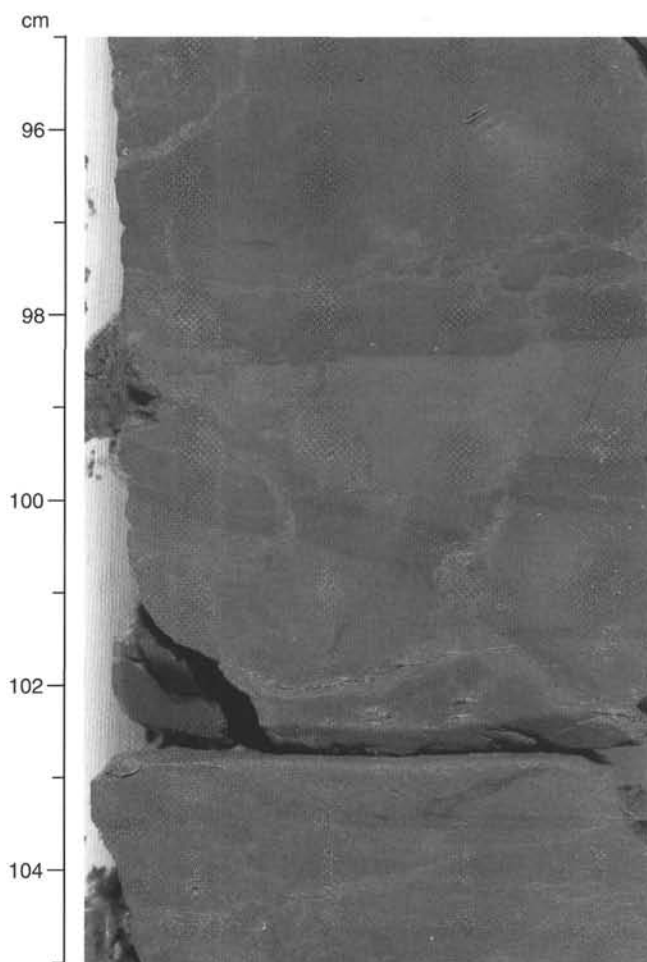


Figure 29. Several funnel-shaped clastic dikes crosscut silty claystone and siltstone; bedding is offset in a normal sense along the dikes. Core 978A-50R-1, 95–105 cm (660.58–660.63 mbsf).

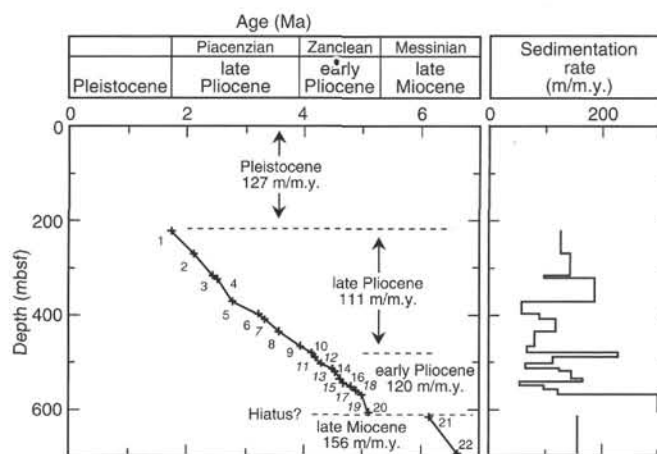


Figure 30. Age-depth model and sedimentation rates at Hole 978A.

First, gas from some deeper origin may have migrated into the unit. Evidence for migration of methane into porous sediments from deeper sources has been found at Sites 762 and 763 on the Exmouth Plateau (off northwest Australia) where a known thermogenic source exists in underlying Jurassic rocks (Meyers and Snowdon, 1993). No comparable source of gas is known in the Alboran Basin. A second

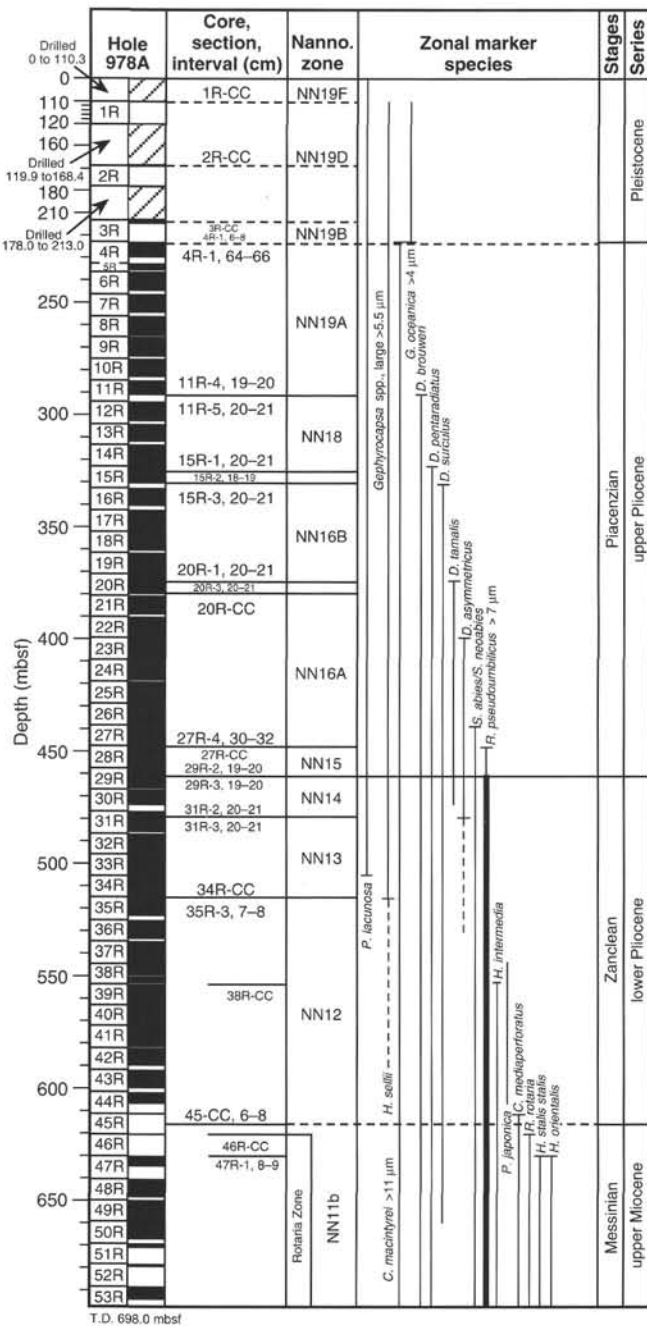


Figure 31. Calcareous nannofossil zonation of Hole 978A. Bold lines represent acme intervals. Lack of a short horizontal line at the end of a species' vertical range line indicates that the range of that species is incomplete. Dashed vertical lines below the Mediterranean bases of *H. sellii* indicate its irregular global occurrence.

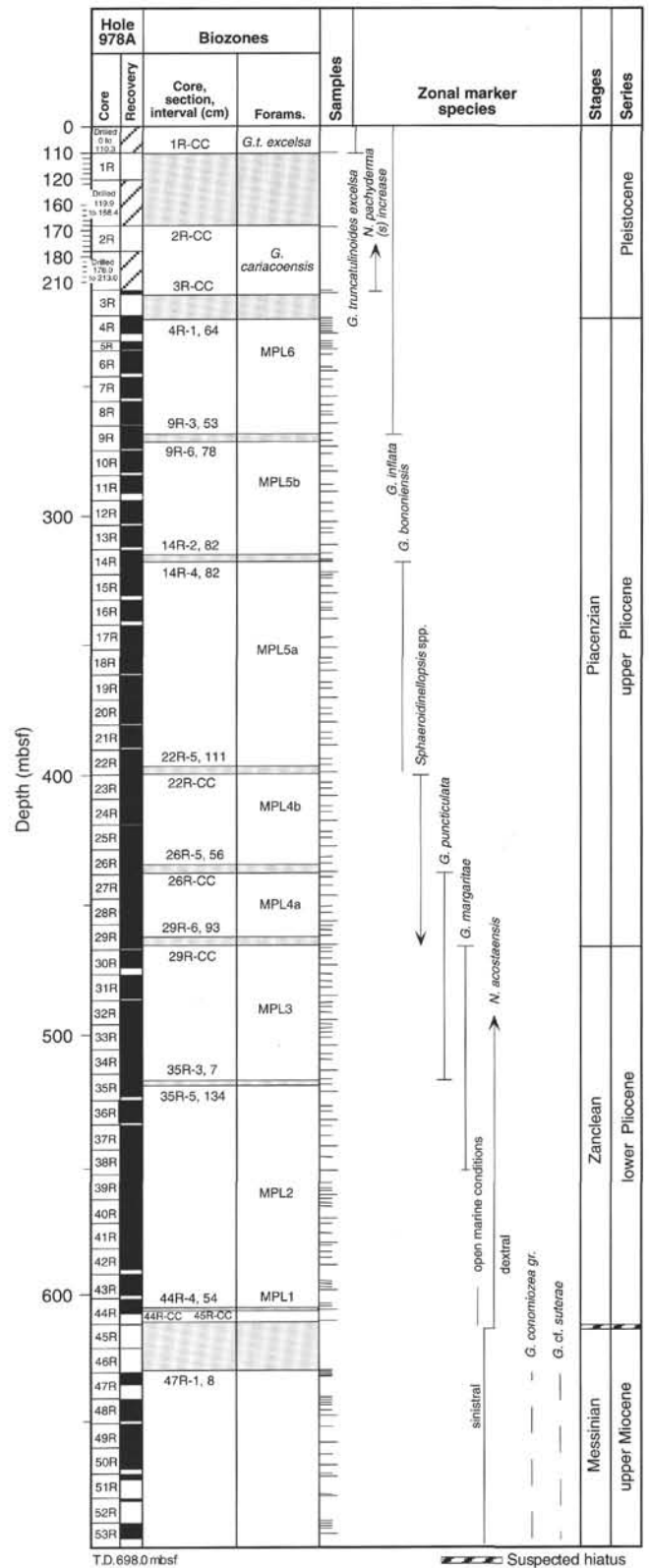


Figure 32. Planktonic foraminiferal zonation of Hole 978A. Shaded areas represent intervals not sampled.

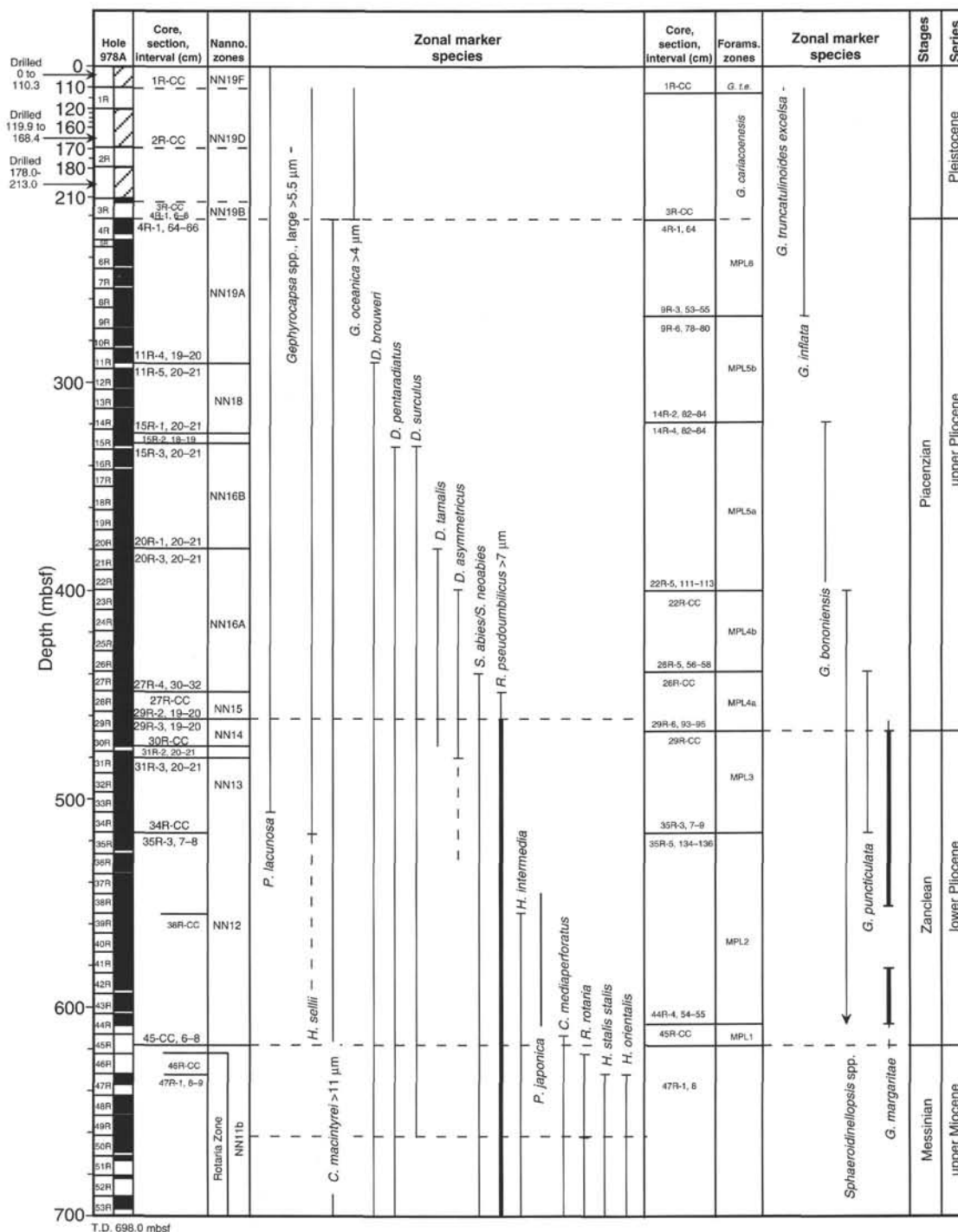


Figure 33. Summary of nannofossil and foraminiferal zonations of Hole 978A. Bold lines represent acme intervals.

possibility is in situ formation by methanogenic bacteria. High C_1/C_2 ratios (Table 7) indicate that the methane is biogenic, as opposed to thermogenic, in origin. The source of the methane is probably from in situ microbial fermentation of the marine organic matter present in the sediments at Site 978. Similar microbial production of methane from marine organic matter has been inferred from high biogenic gas concentrations in Pliocene–Pleistocene sediments from Site 532 on the Walvis Ridge (Meyers and Brassell, 1985), Sites 897 and 898 on the Iberian Abyssal Plain (Meyers and Shaw, in press), Sites 976 and

977 nearby in the Alboran Sea (this volume), and also in middle Miocene sediments from Site 767 in the Celebes Sea (Shipboard Scientific Party, 1990). A biogenic origin of the methane is supported by the marked decrease in headspace methane concentrations at approximately 500 mbsf (Fig. 42), the same sub-bottom depth at which interstitial sulfate reappears (see “Inorganic Geochemistry” section, this chapter). As noted by Claypool and Kvenvolden (1983), the presence of interstitial sulfate inhibits methanogenesis in marine sediments.

Table 3. Age of calcareous nannofossil and planktonic foraminiferal biostratigraphic events and depth of their occurrence in Hole 978A.

		Biostratigraphic event/ magnetostratigraphic data	Age (Ma)	Depth (mbsf)		
				Top	Bottom	Mean
1	FO	<i>G. oceanica</i> >4.0 μ m	1.75	222.76	223.30	223.03
		Pliocene/Pleistocene boundary	1.83		(calculated)	233.13
2	FO	<i>G. inflata</i>	2.13	268.64	273.38	271.01
3	LO	<i>G. bononiensis</i>	2.45	315.42	318.42	316.92
4	LO	<i>D. pentaradiatus/D. surculus</i>	2.52	323.00	324.49	323.74
5	LO	<i>D. tamalis</i>	2.78	371.20	374.21	372.70
6	LO	<i>Sphaeroidinellopsis</i> spp.	3.22	397.31	400.07	398.69
	Base	C2An2n	3.22	400.70	400.70	400.70
7	Top	C2An3n	3.33	408.40	408.40	408.40
8	LO	<i>G. puncticulata</i>	3.57	435.06	438.46	436.76
	Base	C2An3n	3.58	436.00	436.00	436.00
9	LCO	<i>G. margaritae</i>	3.94	465.93	466.70	466.31
10	FCO	<i>D. asymmetricus</i>	4.13	478.40	479.91	479.15
11	Top	C3n1n	4.18	490.60	490.60	490.60
12	Base	C3n1n	4.29	503.10	503.10	503.10
13	Top	C3n2n	4.48	515.40	515.40	515.40
14	FO	<i>G. puncticulata</i>	4.52	518.27	522.54	520.41
15	Base	C3n2n	4.62	535.10	535.10	535.10
16	LO	<i>H. intermedia</i> (very rare occurrence)	4.67	542.40	544.35	543.38
17	Top	C3n3n	4.80	550.30	550.30	550.30
18	Base	C3n3n	4.89	559.20	559.20	559.20
19	Top	C3n4n	4.98	570.20	570.20	570.20
20	FCO	<i>G. margaritae</i>	5.10	605.44	606.74	606.09
21	LO	<i>R. rotaria</i>	6.12	611.39	620.93	616.16
22	FO	<i>R. rotaria</i>	6.62	694.30	694.30	694.30

Notes: FO = first occurrence, LO = last occurrence, LCO = last common occurrence, FCO = first common occurrence; also indicated are the main chronostratigraphic boundaries. This table is also on the CD-ROM, back pocket, this volume.

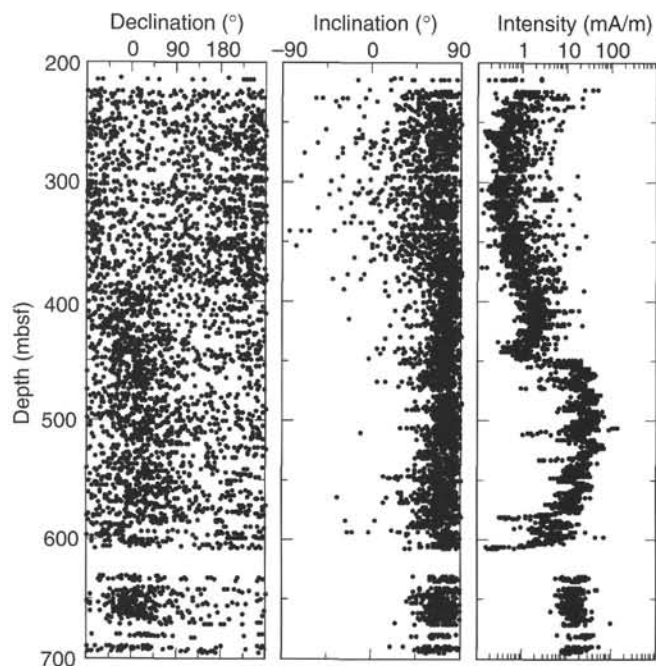


Figure 34. Declination (core-coordinate), inclination, and intensity before demagnetization at Hole 978A.

Higher molecular weight thermogenic headspace gases are also present at Site 978. Concentrations of propane, *iso*-butane, and *iso*-pentane exceed or equal those of ethane in sediments from ~300 to 500 mbsf (Table 7). Ethane is typically the second most abundant component of biogenic gases (Claypool and Kvenvolden, 1983). The unusual gas compositions at Site 978 therefore suggest that the C₃, C₄, and C₅ gases were produced by thermal degradation of sedimentary organic matter during some former period of elevated heat flow in this sub-basin of the Alboran Sea.

INORGANIC GEOCHEMISTRY

Fifteen interstitial water samples were obtained from Hole 978A between 225.60 mbsf to 692.75 mbsf, one sample every five cores until 317.5 mbsf and one every three cores below. Because coring started only below 200 mbsf, early diagenetic processes could not be documented at this site. The most important process influencing the interstitial water composition at Site 978 appears to be upward diffusion of a saline brine.

Evaporite-Related Fluxes

The clearest pattern observed at this site is a downcore increase in salinity, chloride, sodium, and calcium, with a steepening of the concentration gradients below 450 mbsf (Table 8; Figs. 43-46). Sulfate concentrations are close to zero until 450 mbsf and increase steeply below 500 mbsf to reach a constant value of approximately 19 mM below 600 mbsf. Chloride should behave conservatively because it is not involved in any common diagenetic reactions within the sediments. Therefore, chloride concentration gradients are only influenced by fluid diffusion and advection processes and can help to determine the composition of the brine. The linear correlation between sodium and chloride (Fig. 47) suggests that sodium also behaves almost conservatively. The average molar Na/Cl ratio of all the interstitial water samples is 0.82, close to the seawater ratio of 0.86. If halite dissolution were the principal cause of the salinity increase, the Na/Cl ratio would be expected to increase because halite dissolution would move the ratio closer to the stoichiometric ratio of 1. The absence of an increase in this ratio (Fig. 47) indicates that halite dissolution is not responsible for the salinity increase with depth (Fig. 44). Also, because halite salts do not underlie this area, it is possible that the high concentrations of the salt components (Figs. 43-45) are at least partly caused by trapped Messinian-age paleo-seawater. In this basin evaporation may not have been intense enough to cause halite precipitation, but waters with elevated salinities may have seeped into the underlying strata and been preserved in the Pliocene-Pleistocene sediments. Another possible explanation for the high salinities observed at this site is large-scale fluid migration. Important Messin-

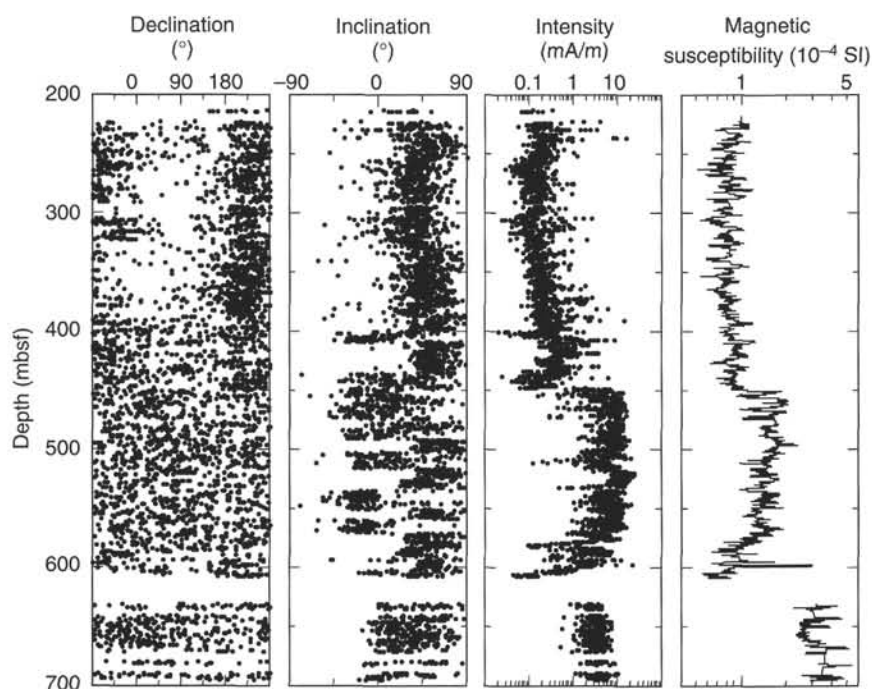


Figure 35. Declination, inclination, and intensity in Hole 978A after AF demagnetization at 15 mT. MST low-field susceptibility after smoothing (20 point).

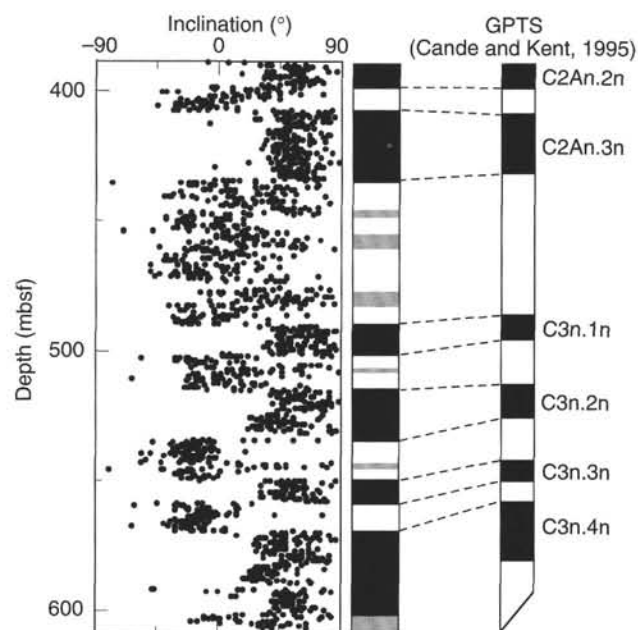


Figure 36. Polarity zones in Hole 978A identified for the interval from 390 to 610 mbsf and possible correlation with GPTS (Cande and Kent, 1995). Gray zones indicate ambiguous polarity intervals after AF demagnetization at 15 mT.

ian halite deposits are known to occur 25 to 30 km east of Site 978 in the South Balearic Basin (Mauffret et al., 1992). Brines produced by the dissolution of these deposits might have migrated along permeable sediment units and influenced the interstitial water composition at this site.

The downcore lithium increase may also be partly related to evaporitic fluids as suggested by the near-linear relationship between Li^+ and Cl^- in the upper part of the section (Fig. 44). Below 500 mbsf these concentration profiles diverge, however, suggesting that lithi-

Table 4. Chron and subchron boundaries.

Depth (mbsf)	Section	Boundary	Age (Ma)
400	22R-7	C2An.2n/C2An.2r	3.22
408	23R-6	C2An.2r/C2An.3n	3.33
436	26R-5/26R-6	C2An.3n/C2Ar	3.58
491	32R-3	C2Ar/C3n.1n	4.18
503	33R-5	C3n.1n/C3n.1r	4.29
515	35R-1	C3n.1r/C3n.2n	4.48
535	37R-1	C3n.2n/C3n.2r	4.62
550	38R-5	C3n.2r/C3n.3n	4.80
559	39R-4	C3n.3n/C3n.3r	4.89
570	40R-5	C3n.3r/C3n.4n	4.98

Notes: Depth (mbsf) and section that includes each chron/subchron boundary is given. Age is after Cande and Kent (1995).

um abundance is affected by other sources and sinks. Lithium replacement in clays by ammonia may be responsible for some of the increase. The potassium concentrations are constant and below seawater values, indicating that no major potassium source is present at depth.

Sulfate concentration in the interstitial waters is also influenced by the postulated brine, but in addition it is controlled by two additional factors: bacterial sulfate reduction and in situ dissolution of gypsum. The absence of sulfate above 450 mbsf can be ascribed to bacterial sulfate reduction, which completely depleted interstitial water sulfate at some time in the past. Down to this depth, organic matter degradation is presently mediated by methanogenic bacteria, as evidenced by the presence of high headspace methane concentrations down to 468 mbsf (see "Organic Geochemistry" section, this chapter). Methanogenic bacteria can favorably compete with sulfate reducers only when sulfate is completely depleted from the environment (Claypool and Kvenvolden, 1983). The constant sulfate concentration below 600 mbsf possibly reflects in situ dissolution of gypsum, although this mineral has been found only in minor amounts in lithostratigraphic Unit II (see "Lithostratigraphy" section, this chapter). The zone between 495 and 606.6 mbsf represents a zone of sulfate reduction, probably due to sulfate-reducing bacteria. The presence of sulfate below 500 mbsf leads to a reduction in bacterio-

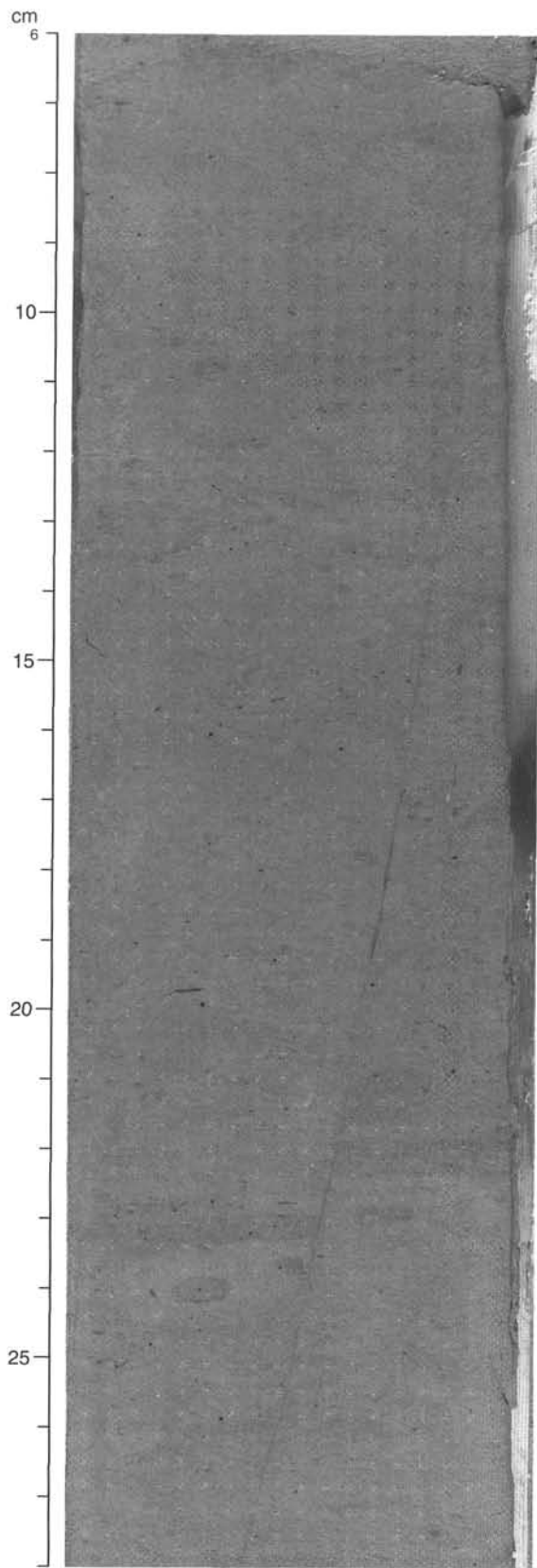


Figure 37. Steep fault in bioturbated semiconsolidated Pliocene? clay with about 1 cm normal displacement. Section 978A-17R-5, 6–28 cm. Note transfer zone at upper right (interval 10–12 cm).

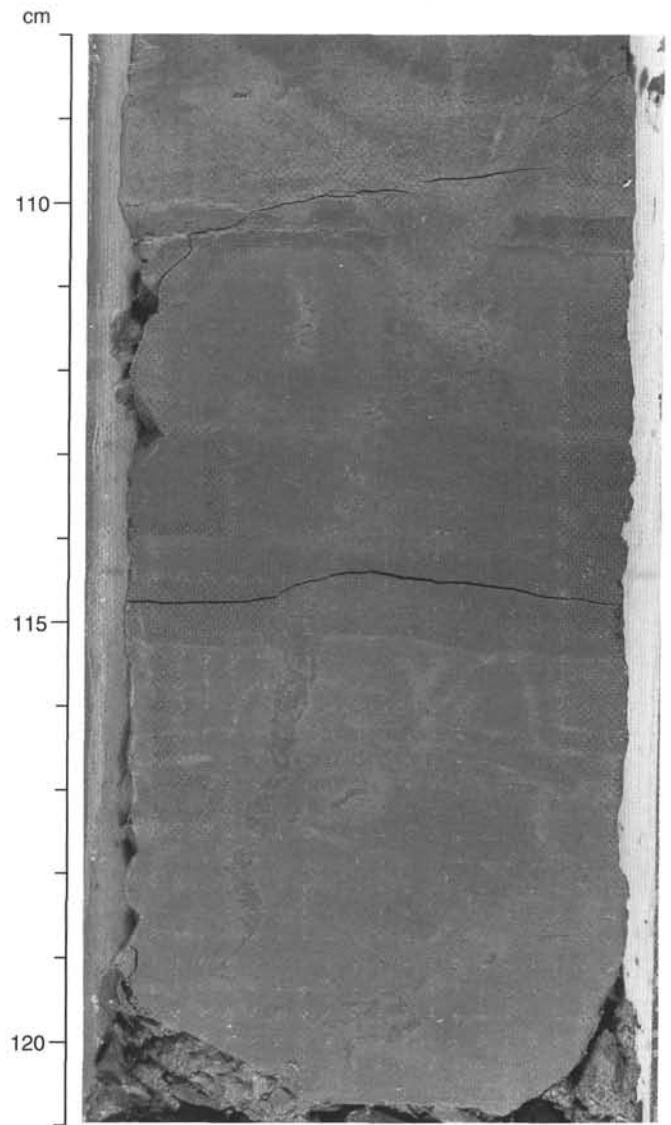


Figure 38. Dilational fractures in well-consolidated late Miocene mudstone. In the fracture at bottom left, note the matching walls of the fracture, the upward increase in the amount of dilation, and the component of displacement down to the left. At the bottom, the displacement is apparently transferred along a bedding-parallel slip surface to another dilational fracture to the right. The fractures are filled with clay and fragments of the surrounding mudstone. Section 978A-50R-1, 108–121 cm.

genic methane production, as shown by the drop in headspace methane concentrations below 470 mbsf (see “Organic Geochemistry” section, this chapter).

Carbonate Diagenesis

Alkalinity was measured on only one sample below 492.2 mbsf because of the low amounts of interstitial water recovered. The alkalinity profile shows a maximum of 3.5 mM at 269.5 mbsf that corresponds with the highest ammonia concentrations and then decreases downcore to concentrations well below average seawater values (Fig. 43B). This may indicate that the rate of organic matter decomposition is highest at that depth and that alkalinity is consumed at depth by carbonate precipitation and/or clay or zeolite formation. The calcium

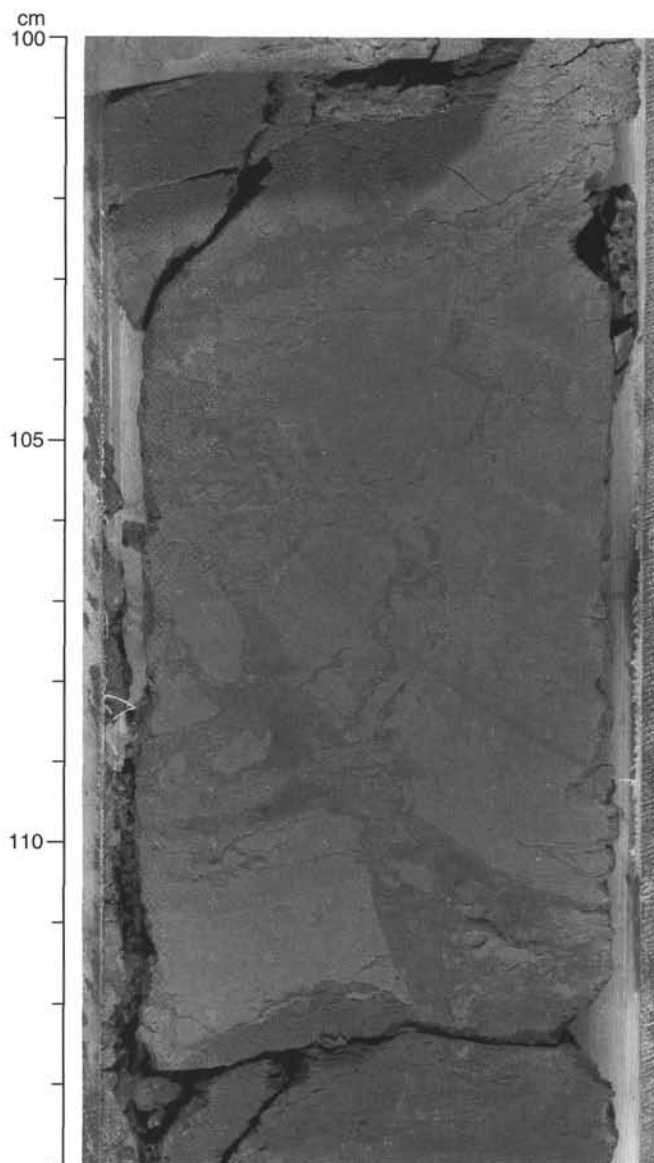


Figure 39. Dilational fractures and brecciation in late Miocene mudstone. Note that most of the fractures have matching walls and that the larger fragments can be fitted back together. The fracture fill appears to be clay derived from the underlying layer, but the relationship is disturbed by a drilling-induced biscuit structure. Section 978A-48R-5, 100–114 cm.

profile is dominated by the evaporite source at depth, whereas magnesium concentrations appear to be more influenced by carbonate diagenesis. Magnesium concentrations are consistently below seawater concentrations, indicating that precipitation of high magnesium calcite or dolomite has occurred in the sediments. The dramatic magnesium increase below 600 mbsf (Fig. 43) suggests that part of the magnesium may be derived from a brine.

The strontium concentration profile, which shows a maximum at 492.20 mbsf, can be explained by carbonate recrystallization. Although biogenic carbonate is not very rich in strontium, its dissolution and inorganic reprecipitation releases strontium to interstitial waters (Manheim and Sayles, 1974). The strontium minimum at 606.05 mbsf suggests the precipitation of a strontium-bearing mineral.

In conclusion, the interstitial water profiles at Site 978 appear to be strongly influenced by the presence of a saline brine, possibly a paleo-fluid trapped below the Pliocene–Pleistocene sediments or derived from large-scale fluid circulation, coupled with the in situ dissolution of gypsum within lithostratigraphic Unit II.

PHYSICAL PROPERTIES

Physical property measurements were made on whole-core sections (for MST and thermal conductivity measurements), split cores (for sonic velocity measurements), and discrete samples (for index properties) for Site 978. Natural gamma ray was measured at 10-cm intervals on cores as part of the MST. MST and thermal conductivity measurements were made on every section. Index properties were measured once per section until Core 978A-32X and every other section from Core 978A-33X onwards. The MST velocity was measured for only the RCB cores. Velocity measurements using DSV and Hamilton frame transducers were made on every section. Results are shown in Figures 48–51.

Some of the physical properties, such as susceptibility (Fig. 48A), bulk density, porosity, and void ratio (Fig. 50; Table 9 on CD-ROM) show a distinctive jump in their values at 460 mbsf. This boundary seen in the physical properties does not correspond to any lithological boundary. Differential lithification could be a possible cause for the formation of this boundary.

In comparing Sites 977 and 978, the thermal conductivity data for Site 977 (Fig. 49) and for Site 978 (Fig. 49 and Table 9 on CD-ROM, back pocket, this volume) lie within same range of values. Also, the velocity values from Site 977 (Fig. 51; Table 9 on CD-ROM) and Site 978 (Fig. 51) show similar trends.

The susceptibility data (Fig. 48) show two maxima, at 460 to 600 mbsf and from 640 mbsf to the bottom of the hole. The first maxima lies in the Pliocene, formation, which contains disseminated pyrite (see “Lithostratigraphy” section, this chapter). The second maxima lies in the Miocene.

The grain densities are almost constant with depth (Fig. 50; Table 10 on CD-ROM, back pocket, this volume), reflecting little change in the composition of sediment input.

A gap in the velocity data between 310–330 mbsf was caused by an instrumentation breakdown (Fig. 51; Table 11 on CD-ROM, back pocket, this volume). Two gradients are observed in the data from 200 mbsf to 540 mbsf and from 540 mbsf to 600 mbsf. A high velocity value of 2.2 km/s occurs at around 320 mbsf in a semi-lithified sand. The data are widely scattered from 630 mbsf to the bottom of the hole. This corresponds to the Miocene Lithostratigraphic Unit III (see “Lithostratigraphy” section, this chapter). This unit consists of calcareous siltstone, calcareous silty claystone, and calcareous silty sandstone.

REFERENCES

- Alonso, B., and Maldonado, A., 1992. Plio-Quaternary margin growth patterns in a complex tectonic setting: northeastern Alboran Sea. *Geo-Mar. Lett.*, 12:137–143.
- Cande, S.C., and Kent, D.V., 1995. Revised calibration of the geomagnetic polarity timescale for the Late Cretaceous and Cenozoic. *J. Geophys. Res.*, 100:6093–6095.
- Claypool, G.E., and Kvenvolden, K.A., 1983. Methane and other hydrocarbon gases in marine sediment. *Annu. Rev. Earth Planet. Sci.*, 11:299–327.
- Colalongo, M.L., Di Grande, A., D’Onofris, S., Giannelli, L., Iaccarino, S., Mazzei, R., Romeo, M., and Salvatorini, G., 1979. Stratigraphy of Late Miocene Italian sections straddling the Tortonian/Messinian boundary. *Boll. Soc. Paleontol. Ital.*, 18:258–302.
- Emerson, S., and Hedges, J.L., 1988. Processes controlling the organic carbon content of open ocean sediments. *Paleoceanography*, 3:621–634.

- Espitalié, J., Laporte, J.L., Leplat, P., Madec, M., Marquis, F., Paulet, J., and Boutefeu, A., 1977. Méthode rapide de caractérisation des roches mères, de leur potentiel pétrolier et de leur degré d'évolution. *Rev. Inst. Fr. Pet.*, 32:23–42.
- Manheim, F.T., and Sayles, F.L., 1974. Composition and origin of interstitial waters of marine sediments, based on deep sea drill cores. In Goldberg, E.D. (Ed.), *The Sea* (Vol. 5): *Marine Chemistry: The Sedimentary Cycle*: New York (Wiley), 527–568.
- Mauffret, A., Maldonado, A., and Campillo, A.C., 1992. Tectonic framework of the Eastern Alboran and Western Algerian Basins, Western Mediterranean. *Geo-Mar. Lett.*, 12:104–110.
- McIver, R.D., 1975. Hydrocarbon occurrences from JOIDES Deep Sea Drilling Project. *Proc. Ninth Petrol. Congr.*, 269–280.
- Meyers, P.A., 1994. Preservation of elemental and isotopic source identification of sedimentary organic matter. *Chem. Geol.*, 144:289–302.
- Meyers, P.A., and Brassell, S.C., 1985. Biogenic gases in sediments deposited since Miocene times on the Walvis Ridge, South Atlantic Ocean. In Caldwell, D.E., Brierley, J.A., and Brierley, C.L. (Eds.), *Planetary Ecology*: New York (Van Nostrand Reinhold), 69–80.
- Meyers, P.A., and Shaw, T.J., 1996. Organic matter accumulation, sulfate reduction, and methanogenesis in Pliocene-Pleistocene turbidites on the Iberia Abyssal Plain. In Whitmarsh, R.B., Sawyer, D.S., Klaus, A., and Masson, D.G. (Eds.), *Proc. ODP, Sci. Results*, 149: College Station, TX (Ocean Drilling Program), 705–712.
- Meyers, P.A., and Snowdon, L.R., 1993. Sources and migration of methane-rich gas in sedimentary rocks on the Exmouth Plateau: northwest Australian continental margin. In Oremland, R.S. (Ed.), *Biogeochemistry of Global Change*: New York (Chapman and Hall), 434–446.
- Pickering, K.T., Hiscott, R., and Hein, F.J., 1989. *Deep-Marine Environments: Clastic Sedimentation and Tectonics*: London (Unwin Hyman).
- Raymo, M.E., Hodell, D., and Jansen, E., 1992. Response of deep ocean circulation to initiation of Northern Hemisphere glaciation (3–2 Ma). *Paleoceanography*, 7:645–672.
- Shipboard Scientific Party, 1990. Site 767. In Rangin, C., Silver, E.A., von Breyman, M.T., et al., *Proc. ODP, Init. Repts.*, 124: College Station, TX (Ocean Drilling Program), 121–193.
- Wright, R., 1978. Neogene paleobathymetry of the Mediterranean based on benthic foraminifers from DSDP Leg 42. In Hsü, K.J., Montadert, L., et al., *Init. Repts. DSDP*, 42 (Pt. 1): Washington (U.S. Govt. Printing Office), 837–846.

Ms 1611R-108

NOTE: For all sites drilled, core-description forms (“barrel sheets”) and core photographs can be found in Section 3, beginning on page 429. Smear-slide data can be found in Section 4, beginning on page 949. Thin-section data can be found in Section 5, beginning on page 991. See Table of Contents for material contained on CD-ROM.

Table 5. Results of inorganic and total carbon (TC) analyses of Pliocene–Pleistocene sediment samples from lithostratigraphic Unit I at Site 978.

Core, section, interval (cm)	Depth (mbsf)	Inorg. C (wt%)	CaCO ₃ (wt%)	TC (wt%)	TOC (wt%)	TN (wt%)	TS (wt%)	C/N
161-978A-								
3R-1, 8–9	213.08	4.53	37.7	4.88	0.35	0.09	0.02	4.54
3R-1, 29–30	213.29	5.23	43.6	5.53	0.30	0.07	0.51	5.00
4R-1, 122–123	223.92	3.05	25.4	3.36	0.31	0.14	0.78	2.58
4R-1, 132–133	224.02	3.51	29.2	3.74	0.23	0.04	0.70	6.71
4R-1, 142–144	224.12	3.76	31.3	4.10	0.34	0.09	1.63	4.41
4R-2, 2–3	224.22	4.00	33.3	4.23	0.23	0.12	0.00	2.24
4R-2, 133–134	225.53	3.48	29.0	3.69	0.21	0.08	0.02	3.06
4R-5, 10–11	228.30	5.11	42.6	5.60	0.49	0.11	0.80	5.20
5R-1, 14–15	232.44	3.94	32.8	4.36	0.42	0.09	1.01	5.44
5R-1, 118–119	233.48	3.90	32.5	4.17	0.27	0.09	0.00	3.50
5R-2, 42–43	234.22	3.48	29.0	3.91	0.43	0.09	0.84	5.57
6R-1, 40–41	236.60	3.95	32.9	4.42	0.47	0.11	0.89	4.98
6R-2, 15–16	237.35	5.19	43.2	5.70	0.51	0.10	0.34	5.95
6R-4, 90–91	241.10	4.81	40.1	5.21	0.40	0.11	0.31	4.24
6R-5, 73–74	242.43	3.99	33.2	4.55	0.56	0.09	0.83	7.26
7R-1, 102–103	246.92	3.55	29.6	4.18	0.63	0.12	1.03	6.13
7R-5, 92–93	252.82	4.88	40.7	5.47	0.59	0.11	0.00	6.26
7R-5, 116–117	253.06	5.46	45.5	5.61	0.15	0.08	0.76	2.19
7R-6, 84–85	254.24	3.86	32.2	4.26	0.40	0.08	0.94	5.83
8R-1, 37–38	255.87	3.26	27.2	3.71	0.45	0.09	1.15	5.83
8R-1, 86–87	256.36	4.69	39.1	4.91	0.22	0.12	0.00	2.14
8R-3, 23–24	258.73	3.84	32.0	4.22	0.38	0.09	1.01	4.93
8R-3, 114–115	259.64	5.22	43.5	4.96	0.00	0.09	0.56	0.00
9R-1, 95–96	266.05	5.08	42.3	5.53	0.45	0.09	0.80	5.83
9R-5, 10–11	271.20	3.68	30.7	4.02	0.34	0.08	0.43	4.96
9R-6, 18–19	272.78	4.28	35.7	5.15	0.87	0.10	0.88	10.15
10R-1, 108–109	275.88	5.52	46.0	5.92	0.40	0.07	0.19	6.67
10R-2, 53–54	276.83	5.92	49.3	6.18	0.26	0.09	0.71	3.37
10R-3, 42–43	278.22	4.30	35.8	4.65	0.35	0.09	1.22	4.54
11R-1, 145–146	285.75	3.53	29.4	4.03	0.50	0.06	0.00	9.72
11R-2, 48–49	286.28	4.61	38.4	4.91	0.30	0.09	0.00	3.89
11R-3, 120–121	288.50	3.62	30.2	4.24	0.62	0.13	1.45	5.56
11R-5, 5–6	290.35	6.08	50.6	6.35	0.27	0.07	0.00	4.50
12R-1, 63–64	294.53	5.14	42.8	5.56	0.42	0.06	0.00	8.17
12R-3, 55–56	297.45	5.99	49.9	6.47	0.48	0.10	0.38	5.60
12R-4, 95–96	299.35	5.12	42.6	5.48	0.36	0.11	0.65	3.82
12R-5, 105–106	300.95	4.69	39.1	5.08	0.39	0.11	0.62	4.14
13R-3, 33–34	306.93	5.61	46.7	6.05	0.44	0.10	0.00	5.13
13R-6, 40–42	311.50	5.31	44.2	5.74	0.43	0.09	0.71	5.57
14R-3, 33–34	316.43	4.79	39.9	5.22	0.43	0.13	0.64	3.86
14R-5, 13–14	319.23	5.33	44.4	5.74	0.41	0.09	0.34	5.31
14R-6, 40–41	321.00	5.18	43.1	5.61	0.43	0.09	0.00	5.57
14R-7, 10–11	322.20	4.98	41.5	5.47	0.49	0.11	0.77	5.20
15R-1, 32–33	323.12	4.07	33.9	4.48	0.41	0.12	0.45	3.99
15R-3, 87–88	326.67	4.91	40.9	5.39	0.48	0.12	0.09	4.67
15R-4, 50–51	327.80	4.70	39.2	5.02	0.32	0.01	0.34	37.33
15R-5, 100–101	329.80	5.28	44.0	5.90	0.62	0.14	1.32	5.17
16R-1, 16–17	332.66	4.99	41.6	5.42	0.43	0.11	0.42	4.56
16R-4, 75–76	337.75	5.37	44.7	5.73	0.36	0.06	0.29	7.00
16R-4, 137–138	338.37	3.33	27.7	3.92	0.59	0.14	0.69	4.92
16R-5, 84–85	339.34	4.05	33.7	4.39	0.34	0.12	0.00	3.31

Table 5 (continued).

Core, section, interval (cm)	Depth (mbsf)	Inorg. C (wt%)	CaCO ₃ (wt%)	TC (wt%)	TOC (wt%)	TN (wt%)	TS (wt%)	C/N
17R-1, 115-116	343.35	4.93	41.1	5.32	0.39	0.01	0.02	45.50
17R-3, 16-17	345.36	4.58	38.2	4.78	0.20	0.12	0.17	1.94
19R-5, 117-119	368.57	4.88	40.7	5.25	0.37	0.12	0.04	3.60
19R-6, 106-108	369.96	5.23	43.6	5.70	0.47	0.06	0.16	9.14
20R-1, 128-129	372.28	5.01	41.7	5.52	0.51	0.06	0.84	9.92
20R-4, 62-63	376.12	4.33	36.1	4.66	0.33	0.11	0.37	3.50
21R-4, 116-117	386.26	5.57	46.4	6.02	0.45	0.06	0.47	8.75
22R-1, 93-94	391.13	4.89	40.7	5.28	0.39	0.06	0.05	7.58
22R-2, 14-15	391.84	4.31	35.9	4.84	0.53	0.07	0.45	8.83
22R-5, 108-109	397.28	5.53	46.1	5.88	0.35	0.11	0.00	3.71
23R-1, 123-124	401.03	4.90	40.8	5.41	0.51	0.11	0.10	5.41
23R-3, 29-30	403.09	5.69	47.4	6.07	0.38	0.05	0.05	8.87
23R-6, 29-30	407.59	5.61	46.7	5.92	0.31	0.05	0.92	7.23
24R-1, 90-91	410.20	4.76	39.7	5.20	0.44	0.07	1.28	7.33
24R-3, 66-67	412.96	5.59	46.6	5.16	0.00	0.12	0.02	0.00
24R-3, 91-92	413.21	5.92	49.3	6.14	0.22	0.05	0.10	5.13
25R-1, 82-83	419.72	4.50	37.5	4.92	0.42	0.07	0.00	7.00
25R-2, 140-141	421.80	4.82	40.2	5.21	0.39	0.07	0.06	6.50
25R-5, 90-91	425.80	6.55	54.6	6.86	0.31	0.05	0.00	7.23
25R-6, 23-24	426.63	5.02	41.8	5.50	0.48	0.12	0.09	4.67
26R-1, 15-16	428.65	4.40	36.7	4.83	0.43	0.07	0.05	7.17
26R-2, 60-61	430.60	4.74	39.5	5.22	0.48	0.07	0.50	8.00
26R-4, 70-71	433.70	4.11	34.2	4.75	0.64	0.08	0.61	9.33
26R-5, 58-59	435.08	6.33	52.7	6.87	0.54	0.05	0.09	12.60
27R-1, 89-90	438.99	5.09	42.4	5.58	0.49	0.07	0.18	8.17
27R-4, 76-77	443.36	6.57	54.7	6.94	0.37	0.05	0.06	8.63
27R-7, 51-52	447.61	4.89	40.7	5.27	0.38	0.12	0.07	3.69
28R-3, 84-85	451.64	4.91	40.9	5.36	0.45	0.06	0.00	8.75
28R-4, 112-114	453.42	6.59	54.9	6.77	0.18	0.04	0.13	5.25
28R-5, 60-62	454.40	4.98	41.5	5.39	0.41	0.06	0.00	7.97
28R-6, 57-59	455.87	7.13	59.4	7.44	0.31	0.04	0.00	9.04
29R-1, 44-45	457.94	4.73	39.4	5.02	0.29	0.05	0.00	6.77
29R-3, 91-92	461.41	5.05	42.1	5.38	0.33	0.06	0.04	6.42
29R-4, 76-77	462.76	6.56	54.6					
29R-7, 11-12	466.41	5.53	46.1	5.90	0.37	0.06	0.58	7.19
30R-1, 119-120	468.29	6.05	50.4	6.29	0.24	0.05	2.33	5.60
30R-4, 46-47	472.06	4.62	38.5	4.94	0.32	0.07	1.02	5.33
31R-2, 61-62	478.81	5.03	41.9	5.37	0.34	0.06	1.19	6.61
31R-2, 102-103	479.22	6.79	56.6	6.86	0.07	0.05	0.00	1.63
31R-4, 75-76	481.71	6.23	51.9	6.46	0.23	0.05	0.00	5.37
32R-2, 60-62	488.40	6.69	55.7	6.94	0.25	0.04	0.06	7.29
32R-3, 52-53	489.92	4.65	38.7	5.04	0.39	0.07	0.81	6.50
32R-CC, 10-12	496.06	4.49	37.4	4.78	0.29	0.07	0.55	4.83
33R-2, 65-66	498.05	5.90	49.1	6.08	0.18	0.05	0.00	4.20
33R-3, 60-61	499.50	5.11	42.6	5.40	0.29	0.07	0.00	4.83
34R-1, 38-39	505.88	5.06	42.1	5.42	0.36	0.07	1.03	6.00
34R-3, 127-128	509.77	6.64	55.3	6.88	0.24	4.67	0.00	0.06
35R-3, 84-85	519.04	4.83	40.2	5.14	0.31	0.07	1.04	5.17
35R-4, 104-105	520.74	6.69	55.7	6.86	0.17	0.04	0.65	4.96
35R-6, 90-91	523.60	4.22	35.2	4.63	0.41	0.13	1.19	3.68
36R-2, 19-20	526.59	4.49	37.4	5.08	0.59	0.07	1.74	9.83
36R-3, 55-56	528.45	6.70	55.8	6.92	0.22	0.04	0.18	6.42
37R-4, 37-38	539.37	6.61	55.1	6.76	0.15	0.05	0.16	3.50
37R-5, 59-60	541.09	4.69	39.1	5.12	0.43	0.08	0.39	6.27
38R-2, 93-94	546.53	4.82	40.2	5.14	0.32	0.07	0.51	5.33
38R-5, 24-25	550.34	7.32	61.0	7.45	0.13	0.04	0.09	3.79
39R-3, 76-77	557.46	6.70	55.8	6.86	0.16	0.05	0.03	3.73
39R-5, 42-43	560.12	5.12	42.6	5.50	0.38	0.07	0.45	6.33
40R-3, 10-11	566.40	6.94	57.8	7.11	0.17	0.03	0.06	6.61
40R-3, 131-133	567.61	4.24	35.3	4.71	0.47	0.08	0.71	6.85
40R-5, 135-137	570.65	4.39	36.6	4.74	0.35	0.08	0.34	5.10
40R-7, 6-8	572.36	7.04	58.6	7.37	0.33	0.05	0.06	7.70
41R-1, 100-101	573.80	6.98	58.1	7.13	0.15	0.04	0.10	4.37
41R-3, 45-46	576.25	3.22	26.8	3.56	0.34	0.08	0.59	4.96
41R-6, 24-25	580.54	4.63	38.6	5.16	0.53	0.08	0.39	7.73
42R-3, 46-47	585.96	5.08	42.3	5.47	0.39	0.07	0.83	6.50
42R-4, 41-42	587.41	7.13	59.4	7.28	0.15	0.04	0.09	4.38
42R-5, 108-110	589.58	2.97	24.7	3.42	0.45	0.08	0.87	6.56
43R-1, 63-65	592.73	4.54	37.8	4.90	0.36	0.07	0.64	6.00
43R-2, 10-12	593.70	3.12	26.0	3.17	0.05	0.04	0.00	1.46
43R-3, 39-41	595.49	7.27	60.6	7.43	0.16	0.03	0.05	6.22
43R-4, 24-25	596.84	0.58	4.8	0.73	0.15	0.02	0.10	8.75
43R-6, 62-64	600.22	6.88	57.3	7.11	0.23	0.04	0.03	6.71
44R-1, 60-61	602.30	7.19	59.9	7.39	0.20	0.04	0.05	5.83
44R-3, 50-51	605.20	7.65	63.7	8.01	0.36	0.04	0.00	10.50
44R-3, 97-98	605.67	4.42	36.8	4.83	0.41	0.07	0.82	6.83
44R-CC, 12-13	607.40	7.98	66.5	8.23	0.25	0.04	0.08	7.29
47R-1, 15-16	630.75	2.37	19.7	2.46	0.09	0.03	0.00	3.50
47R-1, 47-48	631.07	2.19	18.2	2.25	0.06	0.04	0.00	1.75
47R-1, 59-60	631.19	2.48	20.7	2.63	0.15	0.04	1.60	4.38
47R-2, 66-67	632.76	3.33	27.7	3.50	0.17	0.04	0.00	4.96
47R-2, 140-141	633.50	2.31	19.2	2.39	0.08	0.04	0.00	2.33
47R-3, 131-132	634.91	2.98	24.8	3.13	0.15	0.06	0.00	2.92
47R-CC, 10-11	635.03	2.14	17.8	2.23	0.09	0.06	0.00	1.75
48R-1, 115-116	641.45	3.34	27.8					

Table 5 (continued).

Core, section, interval (cm)	Depth (mbsf)	Inorg. C (wt%)	CaCO ₃ (wt%)	TC (wt%)	TOC (wt%)	TN (wt%)	TS (wt%)	C/N
48R-3, 78-79	644.08	3.41	28.4	4.68	1.27	0.05	0.00	29.63
48R-4, 90-91	645.70	3.37	28.1	3.53	0.16	0.06	0.00	3.11
48R-4, 94-95	645.74	2.98	24.8	3.36	0.38	0.05	0.00	8.87
48R-4, 139-140	646.19	2.18	18.2	2.59	0.41	0.06	0.00	7.97
49R-1, 118-119	651.08	2.94	24.5	3.22	0.28	0.07	0.00	4.67
49R-3, 29-30	653.19	3.15	26.2	3.28	0.13	0.03	0.00	5.06
49R-3, 38-39	653.28	2.89	24.1	3.17	0.28	0.07	1.10	4.67
49R-4, 69-70	655.09	2.18	18.2	2.45	0.27	0.05	0.00	6.30
49R-6, 35-36	657.75	4.58	38.2	4.77	0.19	0.05	0.00	4.43
50R-2, 24-25	661.34	1.89	15.7	2.06	0.17	0.07	0.00	2.83
50R-3, 76-77	663.36	2.89	24.1	3.26	0.37	0.06	0.03	7.19
50R-5, 16-18	665.76	1.82	15.2	2.14	0.32	0.07	3.48	5.33
50R-5, 27-28	665.87	3.71	30.9	3.79	0.08	0.02	0.01	4.67
51R-1, 113-114	670.33	1.69	14.1	1.91	0.22	0.06	3.14	4.28
51R-2, 51-52	671.21	3.05	25.4	3.16	0.11	0.03	0.00	4.28
52R-1, 76-77	679.56	1.91	15.9	2.13	0.22	0.06	0.00	4.28
52R-2, 27-28	680.57	2.18	18.2	2.38	0.20	0.04	0.00	5.83
52R-2, 99-100	681.29	2.39	19.9	2.79	0.40	0.06	0.11	7.78
53R-1, 58-59	688.99	1.82	15.2	2.12	0.30	0.06	3.23	5.83
53R-2, 76-77	690.66	3.24	27.0	3.41	0.17	0.04	0.00	4.96
53R-2, 133-134	691.23	3.80	31.7	3.89	0.09	0.03	0.00	3.50
53R-2, 135-136	691.25	2.54	21.2	2.81	0.27	0.05	2.57	6.30
53R-3, 9-10	691.49	3.59	29.9					
53R-4, 49-50	693.39	2.20	18.3	2.36	0.16	0.05	0.00	3.73
53R-CC, 8-9	694.25	2.34	19.5	2.52	0.18	0.04	0.00	5.25

Notes: Total organic carbon (TOC) concentrations are calculated from the difference between inorganic carbon and TC concentrations. C/N ratios are calculated from TOC and total nitrogen (TN) concentrations and are given as atom/atom ratios. TS = total sulfur concentration. This table is also on the CD-ROM, back pocket, this volume.

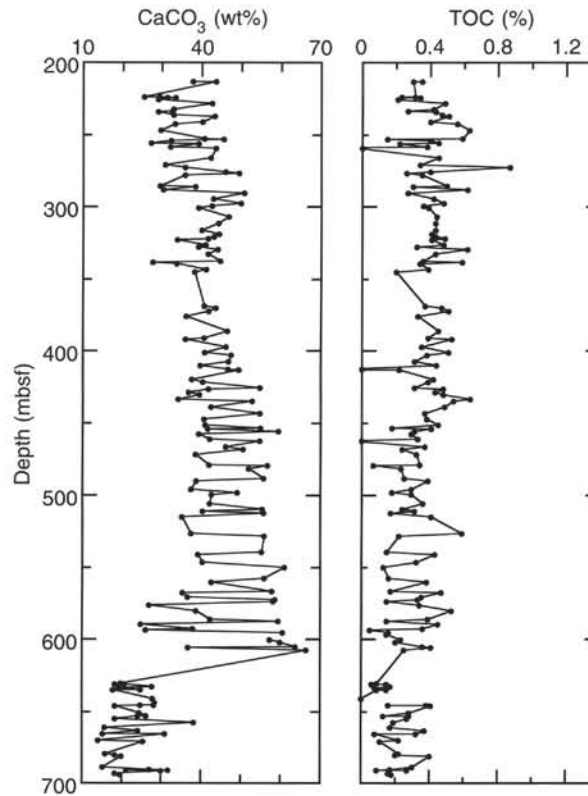


Figure 40. Organic carbon and CaCO₃ concentrations in sediment samples from Hole 978A.

Table 6. Results of Rock-Eval pyrolysis analyses of organic-rich samples selected from Hole 978A.

Core, section, interval (cm)	Depth (mbsf)	TOC (%)	T _{max} (°C)	S ₁	S ₂	S ₃	PI	S ₂ /S ₃	PC	HI	OI
161-978A-											
6R-5, 73-74	242.43	0.40		0.00	0.64	1.45	0.00	0.44	0.05	160	362
7R-1, 102-103	246.92	0.56		0.13	0.88	1.41	0.13	0.62	0.08	157	251
9R-6, 18-19	272.78	0.36		0.02	0.47	1.45	0.04	0.32	0.04	130	402
11R-3, 120-121	288.50	0.54		0.02	0.92	1.49	0.02	0.61	0.07	170	275
15R-5, 100-101	329.80	0.64		0.17	1.46	1.36	0.10	1.07	0.13	228	212
20R-1, 128-129	372.28	0.46		0.01	0.68	1.51	0.01	0.45	0.05	147	328
26R-4, 70-71	433.70	0.46		0.00	0.73	1.56	0.00	0.46	0.06	158	339
36R-2, 19-20	526.59	0.68	487	0.06	0.60	1.21	0.09	0.49	0.05	88	177
41R-6, 24-25	580.24	0.67	442	0.01	0.52	1.07	0.02	0.48	0.04	77	159
48R-3, 78-79	644.08	0.13		0.03	0.39	0.78	0.07	0.50	0.03	300	600
50R-2, 24-25	661.34	0.27		0.10	0.83	0.83	0.11	1.00	0.07	307	307
53R-2, 133-134	691.23	0.10		0.04	0.57	0.70	0.07	0.81	0.05	570	700

Notes: Total organic carbon (TOC) concentrations are derived from the Rock-Eval parameters and therefore differ somewhat from the TOC values of the same samples in Table 5. T_{max} values could not be measured accurately for samples with low (<0.5%) TOC contents. Units of the various Rock-Eval parameters are given in the "Explanatory Notes" chapter (this volume).

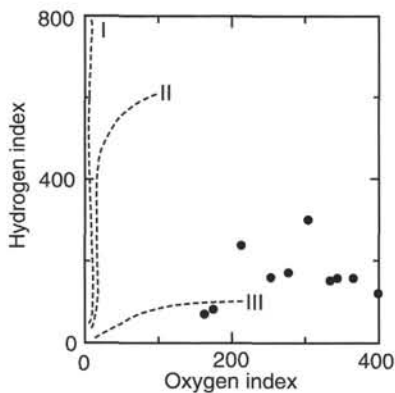


Figure 41. Rock-Eval van Krevelen-type diagram of Pleistocene sapropels from Hole 978A. Organic matter appears to be a mixture of Type II algal material that has been variably oxidized and Type III continental or detrital organic matter. Hydrogen index = mg hydrocarbons/g organic carbon; oxygen index = mg CO₂/g organic carbon.

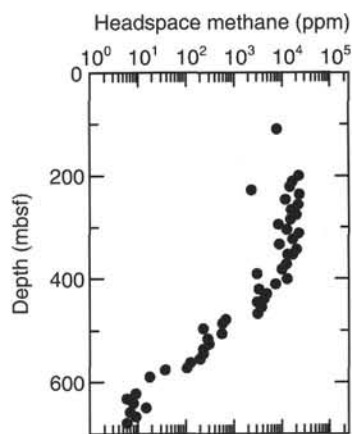


Figure 42. Headspace methane concentrations in sediments from Hole 978A. Interstitial sulfate concentrations begin to increase where methane virtually disappears at 500 mbsf.

Table 7. Results of headspace gas analyses of sediments from Hole 978A.

Core, section, interval (cm)	Depth (mbsf)	C ₁	C ₂	C ₃	IC ₄	IC ₅	C ₁ /C ₂
161-978A-							
1R-CC, 0-5	109	8063					
3R-1, 0-5	200	22527	5				4505
4R-3, 0-5	212	16543	4				4136
5R-2, 0-5	221	14489	4				3622
6R-4, 0-5	228	2287	7				327
7R-4, 0-5	237	23123	7				3303
8R-4, 0-5	247	11764	3				3921
9R-4, 0-5	257	21715	6				3619
10R-4, 0-5	266	15796	5				3159
11R-4, 0-5	276	19999	7				2857
12R-4, 0-5	285	15281	5				3056
13R-4, 0-5	295	8364	3				2788
14R-4, 0-5	305	12777	4				3194
15R-3, 0-5	313	22561	10	13			2256
16R-3, 0-5	323	17387	7	21			2484
17R-4, 0-5	334	8930	4	16			2233
18R-4, 0-5	343	20710	10	77	9	8	2071
19R-4, 0-5	353	13487	6	59	6	5	2248
20R-4, 0-5	353	17345	9	91	9	6	1927
21R-4, 0-5	372	12407	6	53	5		2068
22R-4, 0-5	382	10315	5	59			2063
23R-4, 0-5	391	3083	2	28			1542
24R-4, 0-5	401	12877	7	72	6		1840
25R-4, 0-5	410	7560	5	54	4		1512
26R-4, 0-5	420	3293	2	33			1647
27R-4, 0-5	430	4818	3	32			1606
28R-4, 0-5	439	4300	3	32			1433
29R-2, 0-5	446	3080	3	29			1027
30R-2, 0-5	456	3816	3	34			1272
31R-4, 0-5	468	3155	4	37			789
32R-5, 0-5	479	673		11			
33R-4, 0-5	487	575		9			
34R-4, 0-5	497	231	5				46
35R-4, 0-5	507	565	2	7			283
36R-4, 0-5	516	289	7				41
37R-4, 0-5	526	306	3				102
38R-4, 0-5	536	233	3				78
39R-4, 0-5	545	232	2				116
40R-4, 0-5	555	198	3				66
41R-3, 0-5	563	123	2				62
42R-3, 0-5	573	106					
43R-3, 0-5	576	38					
44R-2, 0-5	590	18					
47R-4, 0-5	622	9					
48R-4, 0-5	632	6					
49R-4, 0-5	641	8					
50R-3, 0-5	650	15					
51R-2, 0-5	658	7					
52R-2, 0-5	667	9					
53R-4, 0-5	680	6					

Notes: Dominance of methane in sediments above 500 mbsf indicates that most of the gases originate from in situ fermentation of organic matter. The presence of significant amounts of thermogenic C₃, C₄, and C₅ gases below 300 mbsf suggests that heat flows were once higher at Site 978.

Table 8. Interstitial water data from Hole 978A.

Core, section, interval (cm)	Depth (mbsf)	pH	Alkalinity (mM)	Salinity (‰)	Cl (mM)	Ca (mM)	Mg (mM)	Mn (µM)	Sr (µM)	SO ₄ (mM)	NH ₄ (µM)	H ₄ SiO ₄ (µM)	Li (µM)	Na (mM)	K (mM)	PO ₄ (µM)
161-978A-																
4R-2, 140-150	225.60	7.4	2.091	38	686	13.0	35.8	4.5	498	0.01	3134	307.27	126	574	5.31	<2.5
9R-3, 140-150	269.50	7.3	3.509	42	726	15.2	35.6	3.5	670	0.24	3362	247.07	146	602	5.23	<2.5
14R-3, 140-150	317.50	7.2	2.547	42	747	18.3	32.3	3.5	914	0.27	3466	221.28	169	584	4.80	<2.5
17R-3, 140-150	346.60	7.3	1.709	45	780	22.2	33.5	4	1167	0.00	3371	238.47	181	607	4.43	<2.5
20R-3, 140-150	375.40	7.2	1.85	44	803	25.7	37.2	7	1392	0.00	3034	206.23	201	640	4.94	<2.5
23R-3, 140-150	404.20	7.3	1.437	46	822	29.9	32.6	6.5	1670	0.00	3280	195.48	211	682	4.16	7.51
26R-3, 140-150	432.90	7.2	1.381	46	835	32.8	34.4	5.5	1800	1.40	3012	130.98	230	643	4.32	5.78
29R-1, 140-150	458.90	7.6	0.763	48	884	37.0	35.0	5.5	1950	0.48	2916	103.04	244	719	5.80	5.20
32R-4, 140-150	492.20	7.6	0.554	51	920	42.4	37.3	6.5	2020	0.66	2743	103.04	261	775	4.67	<2.5
35R-3, 140-150	519.60	n.d.	n.d.	52	933	51.1	41.2	7	1725	5.82	2247	184.73	255	815	5.23	<2.5
38R-3, 135-150	548.45	n.d.	n.d.	57	1007	61.3	37.8	7.5	1620	8.37	2443	113.79	250	867	5.05	<2.5
41R-2, 135-150	575.65	7.3	1.04	60	1060	81.0	37.2	8	1395	11.92	1665	137.43	246	879	6.93	<2.5
44R-3, 135-150	606.05	n.d.	n.d.	64	1114	94.3	30.1	49	980	18.56	1511	87.99	194	972	7.05	<2.5
48R-3, 135-150	644.65	n.d.	n.d.	69	1138	99.7	42.5	59	1070	19.45	1265	107.34	242	931	3.96	<2.5
53R-3, 135-150	692.75	n.d.	n.d.	79	1364	132.0	52.5	171	365	19.36	1647	21.34	306	1118	4.31	<2.5

Note: n.d. = not determined. This table is also on the CD-ROM, back pocket, this volume.

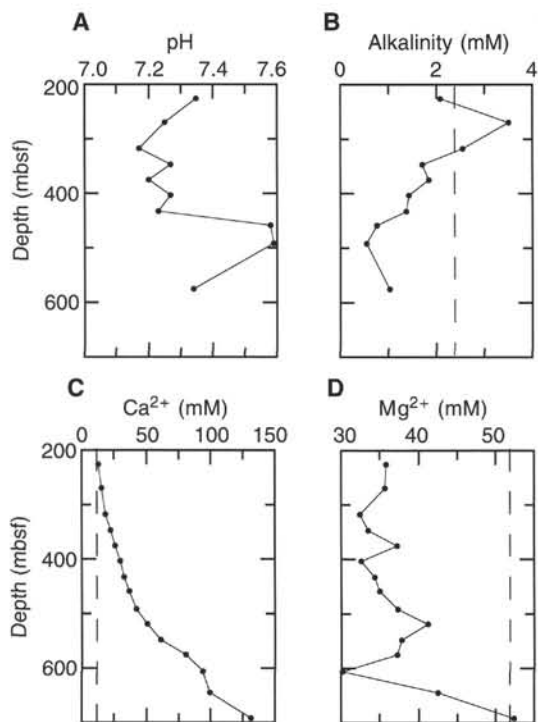


Figure 43. Concentration profiles of (A) pH, (B) alkalinity, (C) calcium, and (D) magnesium in Hole 978A. The dashed lines indicate standard seawater (International Association for the Physical Sciences of the Ocean [IAPSO]) composition.

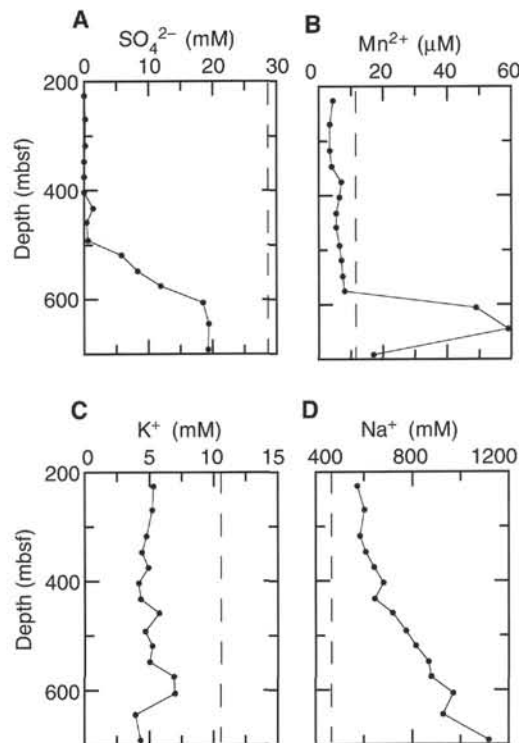


Figure 45. Concentration profiles of (A) sulfate, (B) manganese, (C) potassium, and (D) sodium in Hole 978A. The dashed lines indicate standard seawater (IAPSO) composition.

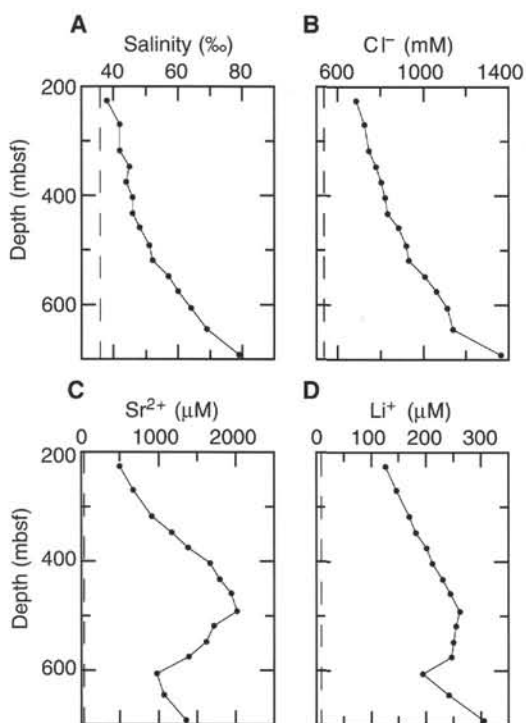


Figure 44. Concentration profiles of (A) salinity, (B) chloride, (C) strontium, and (D) lithium in Hole 978A. The dashed lines indicate standard seawater (IAPSO) composition.

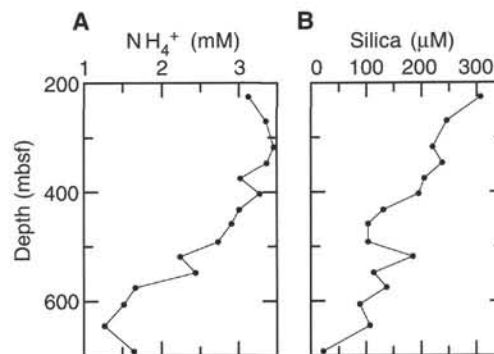


Figure 46. Concentration profiles of (A) ammonium and (B) silica in Hole 978A.

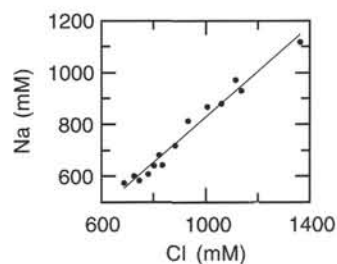


Figure 47. Cross plot of Cl and Na concentrations in Hole 978A showing their linear relationship.

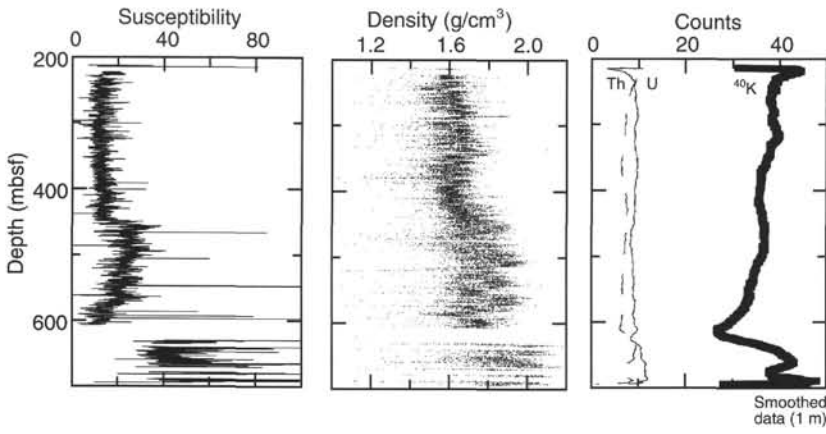


Figure 48. MST data (susceptibility, density, and natural gamma) for Hole 978A.

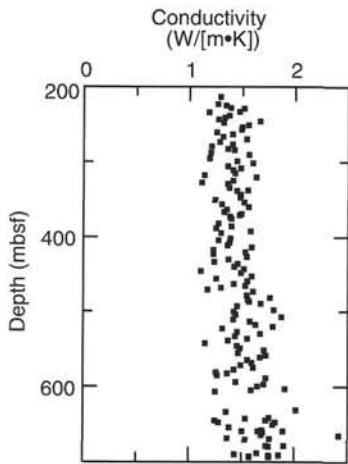


Figure 49. Thermal conductivity data for Hole 978A.

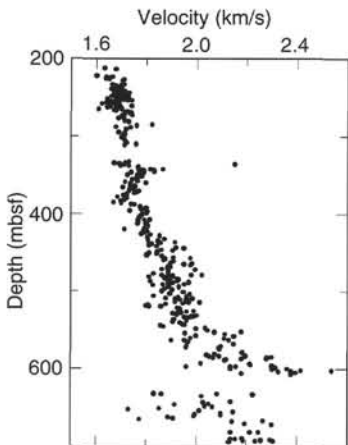


Figure 51. Seismic velocity data for Hole 978A.

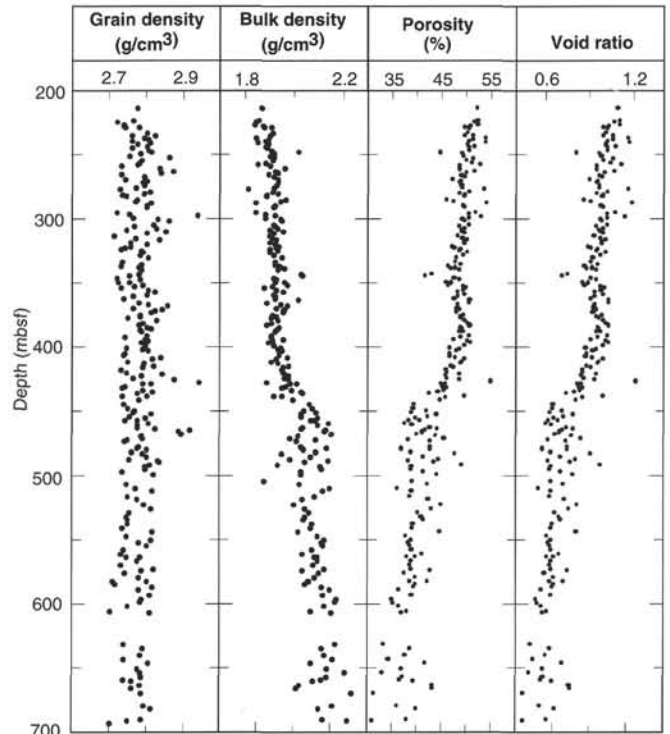


Figure 50. Index property data for Hole 978A.